Optimizing detection and characterization of calcium flickers with deep learning denoising algorithms

Tianxi (Zoe) Zhuang

Department of Physiology

McGill University, Montreal

October 2024

A thesis submitted to McGill University in partial fulfillment of the requirements of the degree of Master of Science in Physiology



©Tianxi Zhuang 2024

Contents

A	Abstract	4
A	Abrégé	5
A	Acknowledgements	7
C	Contributions of Authors	8
	List of Figures and Tables	
Li	List of Abbreviations	10
1	Introduction	12
2	Literature Review	13
	2.1 Overview of calcium signalling in cell migration	
	2.2 Calcium waves and calcium flickers	
	2.3 Calcium imaging	
	2.3.1 Calcium reporter: GCaMP6s	
	2.3.2 Limit of current calcium imaging methods	
	2.3.3 Problems with fast live cell calcium imaging	
	2.4 Calcium Denoising algorithms	
	2.4.1 Conventional denoising algorithms	
	2.4.2 Deep learning calcium denoising algorithms	
	2.4.3 Neuro Imaging via Deep Learning (NIDDL)	
	2.4.4 DeepInterpolation	
	2.4.5 DeepCAD	
3	Methodology	29
	3.1 Cell Culture	
	3.2 Preparation of imaging slides	
	3.3 Cell fixation	
	3.4 Setup of Widefield Calcium Imaging	
	3.5 Calcium Imaging Experiments	
	3.6 Model training	
	3.6.1 NIDDL	
	3.6.2 Deep Interpolation	
	3.6.3 DeepCAD	
	3.7 Model testing.	
	3.7.1 NIDDL	
	3.7.2 Deep Interpolation	
	3.7.3 DeepCAD	
	3.8 Quantification Methods	
	3.8.1 Generation of pseudo high exposure time videos	
	3.8.2 Analysis of the intensity plot	
	3.8.3 Manual counting the number of calcium flickers	
	3.8.4 Automated detection of calcium flickers in denoised videos	
	3.8.5 Calculation of SNR	
	3.8.6 Generation of simulated calcium data	
	•	
4	Results	

	4.1 Deep learning denoising algorithms enhance image SNR better than traditional methods	39
	4.2 DeepCAD is the optimal denoising algorithm	46
	4.3 DeepCAD can push the temporal limit of calcium imaging to 10 ms or 100 fps	55
5	Discussion	57
6	Conclusion	64
Re	eferences	65

Abstract

Calcium ions (Ca²⁺) are highly regulated signaling molecules involved in many aspects of cellular physiology. Transient localized Ca²⁺ signals, also referred to as flickers, are generated upon calcium influx through the mechanosensitive calcium channels located at the plasma membrane such as Piezo 1. In live cell fluorescence imaging, achieving a satisfactory signal-tonoise ratio (SNR) while maintaining cell health often requires a sacrifice in temporal and/or spatial resolution. Since calcium flickers are highly dynamic and they rise and fall within tens of milliseconds, traditional imaging protocols that use 200 ms exposure time to achieve an optimal SNR may miss some small or short-lived flickers. This study aimed to develop an optimized fast calcium image acquisition protocol for the precise identification and characterization of calcium flickers. There are multiple ways of image denoising: mathematical methods including Gaussian and median filters, and deep learning denoising algorithms including NIDDL, Deep Interpolation and DeepCAD. We used widefield imaging to capture calcium flickers in cultured cell monolayers expressing a membrane anchored GCaMP6s fluorescent calcium sensor with stream camera acquisition and different camera exposure times. Manual flicker counts served as ground truth data while an automated flicker detection script was developed to detect and characterize calcium flicker properties. Deep learning denoising models outperformed traditional mathematical filters with less image blurring and higher SNR. Among the three selected deep learning models, DeepCAD was the optimal one. NIDDL generated large square artifacts within the images while Deep Interpolation over corrected images resulting in the loss of low intensity information. DeepCAD achieved the highest SNR, detected the highest number of flickers relative to 200ms flicker counts, was able to detect the highest number of dim calcium flickers, maintained the flicker area relative to long exposure images, allowed more accurate determination of flicker durations and did not generate any apparent image artifacts. The temporal resolution of DeepCAD can be pushed to effectively measure Ca²⁺ flickers at 100 frame per second. It is also straightforward to install, train and implement, making it accessible to life scientists without the need for extensive computer science expertise. Overall, the new calcium image acquisition and analysis protocol developed during this thesis work enables rapid image acquisition for more precise identification and characterization of Ca²⁺ flickers with high spatial and temporal resolution. This work provides an effective protocol and tools to effectively measure and understand the dynamics and characteristics of calcium flickers.

Abrégé

Les ions calcium (Ca²⁺) sont des molécules de signalisation hautement régulées impliquées dans de nombreux aspects de la physiologie cellulaire. Les signaux de calcium localisés et transitoires, appelés scintillements, sont générés par l'influx de calcium à travers les canaux calciques mécanosensibles, tels que Piezo 1, situés dans la membrane plasmique. En imagerie par fluorescence avec des cellules vivantes, atteindre un rapport signal/bruit satisfaisant tout en maintenant la santé des cellules nécessite souvent un sacrifice en termes de résolution temporelle et/ou spatiale. Étant donné que les scintillements de calcium sont très dynamiques et qu'ils apparaissent et disparaissent en quelques dizaines de millisecondes, les protocoles d'imagerie traditionnels utilisant un temps d'exposition d'environ 200 ms pour atteindre un rapport signal/bruit optimal peuvent manquer certains scintillements petits ou de courte durée. Cette étude visait à développer un protocole optimisé d'acquisition rapide d'images de calcium pour l'identification et la caractérisation précises des scintillements de calcium. Il existe plusieurs méthodes de débruitage d'image : des méthodes mathématiques incluant les filtres gaussiens et médians, et des algorithmes de débruitage par apprentissage profond incluant NIDDL, Deep Interpolation et DeepCAD. Nous avons utilisé l'imagerie en épifluorescence pour capturer les scintillements de calcium dans des cellules en culture exprimant un capteur de calcium fluorescent GCaMP6s ancré à la membrane, avec une acquisition de caméra en flux et différents temps d'exposition. Le compte manuel de scintillements a servi comme données de référence puis un script automatisé de détection de scintillements a été développé pour détecter et caractériser les propriétés des scintillements de calcium. Les modèles de débruitage par apprentissage profond ont surpassé les filtres mathématiques traditionnels produisant des images moins floues et des rapport signal/bruit plus élevés. Parmi les trois modèles d'apprentissage profond sélectionnés, DeepCAD était le meilleur. NIDDL a généré de grands artefacts carrés dans les images tandis que Deep Interpolation a corrigé les images de manière excessive, entraînant la perte d'informations de faible intensité. DeepCAD a atteint le rapport signal/bruit le plus élevé, a détecté le plus grand nombre de scintillements par rapport au données de références, a été capable de détecter le plus grand nombre de scintillements de calcium faibles, a maintenu la zone de scintillement par rapport aux images à longue exposition, a permis une détermination plus précise de la durée des scintillements et n'a généré aucun artefact visible dans les images. La résolution temporelle de DeepCAD peut être poussée pour mesurer efficacement les

scintillements de Ca²⁺ à 100 images par seconde. Cet algorithme est également simple à installer, à entraîner et à mettre en œuvre, le rendant accessible aux scientifiques des sciences de la vie sans nécessiter de compétences profondes en informatique. Dans l'ensemble, le nouveau protocole d'acquisition et d'analyse d'images de calcium développé au cours de cette thèse permet une acquisition rapide des images pour une identification et une caractérisation plus précises des scintillements de Ca²⁺ avec une haute résolution spatiale et temporelle. Ce travail fournit un protocole efficace et des outils pour mieux mesurer et comprendre la dynamique et les caractéristiques des scintillements de calcium.

Acknowledgements

I would like to first thank Dr. Claire Brown, who has been an amazing supervisor since I first joined her lab. I appreciate your continuous support and advice on this very multidisciplinary project. Thank you for providing so many resources throughout my graduate studies and encouraging me to go for the internship at Amazon. I feel so fortunate to work under your supervision during my master's study at McGill University. Thank you to my committee members, Dr. Gil Bub, Dr. Arnold Hayer and Dr. Masha Prager-Khoutorsky for your valuable feedback and suggestions on my project. I would like to especially thank our committee member and collaborator Dr. Arnold Hayer for his critical insights on my projects and support on experiments. Thank you to Baishali Mukherjee for teaching me cell culture and preparing cells for me. I am grateful for my lab mates in both the Brown Lab and the Hayer Lab, Jalal Al Rahbani, Alex Nowakowski, Natalie Woo and Baishali Mukherjee, Kian Mavalwala, Rodrigo Migueles Ramirez. Thank you all for your advice and help. I would also like to thank ABIF staff, Joel Ryan and Philip Kesner for training me on the microscope. Special thanks to Joel Ryan for helping me translating the abstract to French. To my friend, thank you for listening to me talk or complain about my project. Finally, I would like to thank my parents for their continuous love and encouragement.

Contributions of Authors

I wrote the entirety of the thesis, performed all the data collection, image analysis and generated all of the figures. The thesis was reviewed and edited by Dr. Brown. I conducted all the experiments for this study. The cells and experiment protocols were provided to me by Baishali Mukherjee from Dr. Arnold Hayer's Laboratory at McGill University. The imaging conditions were planned under the guidance of Dr. Brown. The automatic counting script was adapted from Baishali Mukherjee's code. I wrote all the code used to generate the figures in the results section. I conducted all the setup, training and testing of selected denoising algorithms. Images were collected in the McGill University Advanced BioImaging Facility (ABIF), RRID:SCR_017697. The project was selected for AI4Life open call and I asked them for advice on the NIDDL algorithm.

List of Figures and Tables

Figure 2: The architecture of NIDDL	Figure 1: Calcium signaling at the front of the cell.	15
Figure 4: Architecture of DeepCAD	Figure 2: The architecture of NIDDL.	25
Figure 5: Illustration of automated detection of calcium flickers	Figure 3: The architecture of Deep Interpolation.	26
Figure 6: More noise is observed in calcium images captured with a short exposure time compared to a long exposure time	Figure 4: Architecture of DeepCAD.	28
compared to a long exposure time	Figure 5: Illustration of automated detection of calcium flickers.	36
Figure 7: Median filter improves SNR in noisy images	Figure 6: More noise is observed in calcium images captured with a short exposure time	
Figure 8: DeepCAD and Deep Interpolation enhances the image SNR	compared to a long exposure time.	38
Figure 9: Deep Interpolation denoised results appear as a binary image with default image display properties and NIDDL denoised results corrupted with pure noise	Figure 7: Median filter improves SNR in noisy images.	41
display properties and NIDDL denoised results corrupted with pure noise	Figure 8: DeepCAD and Deep Interpolation enhances the image SNR.	42
Figure 10: SNR ratio among different denoising methods	Figure 9: Deep Interpolation denoised results appear as a binary image with default image	
Figure 11: Deep CAD denoised calcium signals aligned well with pseudo high exposure time videos while Deep Interpolation showed slightly smaller calcium signals	display properties and NIDDL denoised results corrupted with pure noise.	43
videos while Deep Interpolation showed slightly smaller calcium signals	Figure 10: SNR ratio among different denoising methods.	44
Figure 12: Normalized intensity plots among raw and multiple denoised methods	Figure 11: Deep CAD denoised calcium signals aligned well with pseudo high exposure tim	e
Figure 13: Denoising methods detect more dim calcium flickers with longer durations	videos while Deep Interpolation showed slightly smaller calcium signals	46
Figure 14: Denoising algorithms detect more calcium flickers compared to raw data	Figure 12: Normalized intensity plots among raw and multiple denoised methods	48
Figure 15: DeepCAD denoises images captured at a short exposure time of 10ms	Figure 13: Denoising methods detect more dim calcium flickers with longer durations	48
Figure 16: Deep Interpolation and Deep CAD recover the signal from noisy images captured with a 5 ms exposure time but cell shape and background information is not revealed	Figure 14: Denoising algorithms detect more calcium flickers compared to raw data	52
with a 5 ms exposure time but cell shape and background information is not revealed	Figure 15: DeepCAD denoises images captured at a short exposure time of 10ms	52
Table 1: Summary of the General Properties of some Different Calcium Indicators	Figure 16: Deep Interpolation and Deep CAD recover the signal from noisy images captured	1
Table 2: Comparison on difficulty of usage and time required for training and testing among selected denoising algorithms. 34 Table 3: Three selected deep learning calcium denoising algorithms and a summary of their different characteristics. 40 Table 4: Number of total and fast flickers in different videos. 49	with a 5 ms exposure time but cell shape and background information is not revealed	56
Table 2: Comparison on difficulty of usage and time required for training and testing among selected denoising algorithms. 34 Table 3: Three selected deep learning calcium denoising algorithms and a summary of their different characteristics. 40 Table 4: Number of total and fast flickers in different videos. 49		
Table 2: Comparison on difficulty of usage and time required for training and testing among selected denoising algorithms. 34 Table 3: Three selected deep learning calcium denoising algorithms and a summary of their different characteristics. 40 Table 4: Number of total and fast flickers in different videos. 49	Table 1: Summary of the General Properties of some Different Calcium Indicators.	18
Table 3: Three selected deep learning calcium denoising algorithms and a summary of their different characteristics. 40 Table 4: Number of total and fast flickers in different videos. 49	•	
Table 3: Three selected deep learning calcium denoising algorithms and a summary of their different characteristics. 40 Table 4: Number of total and fast flickers in different videos. 49		
different characteristics. 40 Table 4: Number of total and fast flickers in different videos. 49		
Table 4: Number of total and fast flickers in different videos. 49		40

List of Abbreviations

CARE: Content-Aware Image Restoration

CNN: Convolutional Neural Network

CICR: Calcium-Induced Calcium Release

DAG: Diacylglycerol

DRAC: Digital Research Alliance of Canada

ECM: Extracellular Matrix

EGFP: Enhanced Green Fluorescent Protein

ER: Endoplasmic Reticulum

FA: Focal Adhesion

FOV: Field of View

FPS: Frames per Second

fMRI: functional Magnetic Resonance Imaging

GCaMP: Genetically Encoded Calcium Indicator

GPU: Graphics Processing Unit

HDN: Hierarchical DivNoising

HUVEC: Human Umbilical Vein Endothelial Cells

IP3: Inositol Triphosphate

IP3K: Inositol Triphosphate Kinase

IP3R: Inositol Triphosphate Receptor

LIS: Live-cell Imaging Solution

MLCK: Myosin Light Chain Kinase

MIP: Maximum Intensity Plot

NIDDL: Neuro Imaging Denoising via Deep Learning

PBS: Phosphate-Buffered Saline

PKC: Protein Kinase C

PLC: Phospholipase C

ReLU: Rectified Linear Unit

SACs: Stretch-Activated Channels

SERCA: Sarcoplasmic/Endoplasmic Reticulum Ca²⁺ ATPase

SNR: Signal-to-Noise Ratio

TIRF: Total Internal Reflection Fluorescence

TRP: Transient Receptor Potential

1 Introduction

The study on the function, dynamics and downstream binding proteins of calcium flickers is ongoing and constrained by the limit of spatiotemporal resolution of the current calcium imaging protocols. The objective of this study was to develop an optimized calcium imaging protocol with enhanced spatial and temporal resolution and apply denoising to enable the detection and characterization of calcium flickers in a more accurate way.

Rapid calcium imaging with a shorter camera exposure time results in an increased amount of noise in the image data, often making flickers indistinguishable from background making it impossible to measure and interpret calcium signals. To remove the noise and restore the true calcium signals in the sample, three state-of-the-art deep learning-based denoising methods were selected. All of them were designed based on neuronal calcium imaging and have not been tested using endothelial cell monolayer calcium imaging data. Each of them belongs to a different deep learning category (supervised or unsupervised) and is designed based on a separate deep learning model.

The aims of the thesis were to: 1) train the three denoising algorithms with low signal-to noise ratio (SNR) calcium image data from human umbilical vein endothelial cells (HUVECs) (for high SNR calcium image data pseudo high exposure time images were created by adding together consecutive images within a time series); 2) test the three selected denoising algorithms for accuracy of image denoising; 3) validate the best denoising algorithms by testing them on image data and counting and characterizing calcium flickers.

Further exploration of the limit of temporal resolution was tested on the selected optimal denoising algorithms, to determine the temporal limits and determine if ultrafast calcium imaging is possible with the new calcium imaging protocol. By achieving high speed calcium imaging, those fast calcium flickers that are otherwise missed because of time delays between image frames or they are averaged out over long exposure times can be captured. The hypothesize is that application of denoising deep learning algorithms will enable rapid calcium imaging and greater accuracy in detecting and characterizing calcium flickers in cell monolayers.

2 Literature Review

2.1 Overview of calcium signalling in cell migration

Calcium (Ca²⁺) is one of the key chemical elements that is involved in many biological functions. For example, at the organismic level, calcium is the major component of the bone, supporting skeleton mineralization¹. At the tissue level, Ca²⁺ triggers synaptic vesicle exocytosis, leading to the release of neurotransmitters and thereby initiating neuronal signal transmission². Ca²⁺ also regulates contraction of multiple types of muscle including striated and smooth muscle via different signaling pathways³. At the cellular level, Ca²⁺ regulates cell proliferation, migration and invasion^{4,5}. Dysregulated Ca²⁺ signaling has been linked to cancer through the induction of calcium channel alterations, interactions with receptors and remodeling of the extracellular matrix⁶.

Cells can migrate as single cells or as a collective of cells. Migrating cells can move in a directional way in response to diffusible chemicals or ligands⁷, mechanical cues⁸, and substrate-bound chemo-attractants⁹. In single cells, two modes of migration are amoeboid and mesenchymal. Amoeboid migration is mainly characterized by gliding and rapid migration through morphological expansion and contraction, primarily seen in highly motile cells including neutrophils, dendritic cells and lymphocytes¹⁰. These amoeboid cells usually have weak integrinmediated adhesions and some are even integrin-independent^{11,12}. On the other hand, mesenchymal migration involves multiple steps including protrusion at the cell front, adhesion formation, force generation by stress fibers, movement of the cell body forward, disassembly of adhesions at the cell rear and detachment at the rear end. Cells can also move together collectively as a group, remaining connected throughout the process. Leader cells in the front senses the environmental stimuli and follower cells respond to the guidance cues from the leader cells or neighboring cells¹³. In fact, leader cells function in a similar way as the cell front in individual cell migration.

Cell migration involves temporal and spatial coordination of multiple structural components such as actin and myosin^{14,15} and regulatory proteins such as Rac, RhoA and Cdc42^{13,16,17}. Calcium signals regulate directed cell movement through a spatially and temporally regulated dynamic architecture of intracellular calcium dynamics. In migrating cells, cytosolic Ca²⁺ levels are low in the cell front (~30 nM) and high in the cell back (~70 nM)¹⁸. The gradient

is maintained by plasma membrane Ca^{2+} -ATPase pumping Ca^{2+} to the extracellular space with an increased activity in the cell front¹⁹ and voltage-gated L-type Ca^{2+} channels in the cell back to maintain a high level of Ca^{2+20} . Sarcoplasmic/endoplasmic reticulum Ca^{2+} ATPase (SERCA) pumps cytosolic Ca^{2+} into the internal Ca^{2+} storage, endoplasmic reticulum (ER) (~100 μ M), to maintain low cytosolic Ca^{2+} at the cell front. But SERCA is not responsible for maintaining the calcium gradients because dysfunction of SERCA activities results in paradoxical increase of Ca^{2+} gradients¹⁹.

The front of the cell protrudes first by forming lamellipodia and/or filopodia and then can retract slightly introducing tension that leads to new adhesions growing or new adhesions forming and stabilizing²¹ their link to the actin cytoskeleton and extracellular matrix (ECM) mediated through myosin contraction²². Local calcium pulses are generated by rapid Ca²⁺ influx into the cell through stretch-activated channels (SACs), e.g. stretch-activated transient receptor potential channels (TRP) and Piezo channels. Polarized cell surface receptors including G-protein coupled receptors and receptor tyrosine-kinases activate phospholipase C enzyme and generates diacylglycerol (DAG) and inositol triphosphate (IP₃) by hydrolysis of PI (4,5) P₂²³ through IP₃ kinase (IP₃K). IP₃ diffuses and activates IP₃ receptors (IP₃R) located at the ER, which are ligand gated cation channels, to release Ca²⁺ signals from ER. Calcium induced Ca²⁺ release (CICR) is triggered by IP₃R and ryanodine receptors²⁴ (Fig. 1). DAG is a lipid second messenger that recruits protein kinase C (PKC) at the plasma membrane. DAG and Ca²⁺ activates PKC and it plays an important role in modulating actin dynamics²⁵ and multiple signal transduction cascades with different cellular responses ranging from cell migration to division.

The calcium pulses at the front can modulate lamellipodia retraction and adhesion by activation of myosin light chain kinase (MLCK) and myosin II²⁶. Myosin II molecules assemble into bipolar filaments and bind to actin filaments through head domains, which enables conformational changes via ATPase activity to move actin filament and generate force required for protrusions^{27,28}. The cyclic Ca²⁺ channel opening may be triggered by Ca²⁺-induced Ca²⁺ release (CICR), generated by TRPs such as TRPM7²⁹ upon the change of membrane tension¹⁸. Since the affinity between Ca²⁺-calmodulin complexes and MLCK are extremely high³⁰ and the basal cytosolic Ca²⁺ level is extremely low, tiny local Ca²⁺ signals in nanomolar scales are sufficient to regulate myosin activities.

The calcium pulse is depleted by removing calcium signals either back to ER by SERCA or to ECM by PMCA¹⁸. In addition to SERCA, store-operated Ca²⁺ entry replenishes internal Ca²⁺ storage by activating STIM1^{19,31}, which is transported to the ER-plasma membrane junction and open the Ca²⁺ influx channel ORAI1^{18,32}. The Ca²⁺ influx activates the GTPase Arf5 via Ca²⁺-activated guanine nucleotide exchange factor IQSec1, which forms a complex with lipid transfer protein ORP3 and modulate FA disassembly by translocating to ER-plasma membrane contact site close to FAs³³.

In the back, in order to move forwards cells, detach through adhesion disassembly and can move in a directional way. The rear-end retraction is also mediated by myosin II-based actomyosin contraction through Ca^{2+} dependent MLCK. Ca^{2+} dependent protease, calpain 2, cleaves adhesion complex proteins such as FAK, paxillin and talin 1, leading to adhesion complex disassembly and detachment of the cell rear³⁴. Calpain also modulates α -actinin localization into focal contacts and complexes, which is essential in disassembly or translocation of zyxin-containing contact sites³⁵. L-type voltage-gated Ca^{2+} channels have been implicated to support increased Ca^{2+} levels at the trailing edge²⁰, but the detailed regulating mechanism remains unknown.

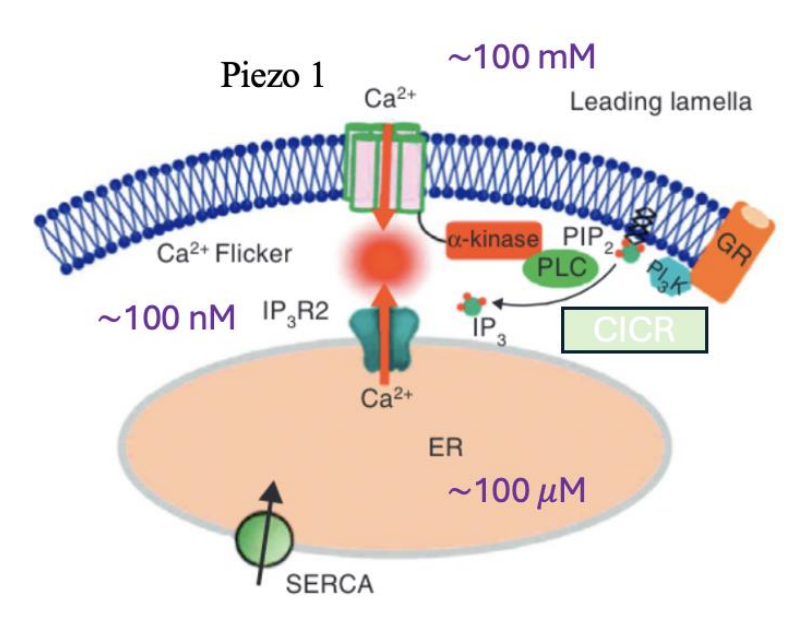


Figure 1: Calcium signaling at the front of the cell. Adapted with permission from Elsevier: Current Opinion in Cell Biology, Calcium gradients underlying cell migration, Chaoliang Wei et al., 2012.

2.2 Calcium waves and calcium flickers

There are two types of calcium signals in migrating cells: calcium waves and calcium flickers. Calcium waves represent the propagation of increases in intracellular Ca²⁺ levels across the cell by Ca²⁺ release through IP₃Rs with amplification from RyRs. They involve coordination of cell communication and multicellular responses³⁶. Calcium flickers, also referred to as calcium pulses²⁶, are generated by Ca²⁺ influx into the cytosol through SACs at the plasma membrane and/or IP₃-mediated Ca²⁺ release from the ER Ca²⁺ storage in response to mechanical force or guidance cues. The widespread Ca²⁺ waves usually last 0.5-1.5 s while transient Ca²⁺ flickers rise and fall within 20 ms to 100 ms³⁷.

In migrating human embryonic lung fibroblasts, calcium flickers are generated by TRPM7 channels and are most active at the leading lamella, promoting the turning of fibroblasts³⁸. Calcium release from the ER increases the amplitude of calcium flickers but does not contribute to the frequency of calcium formation³⁸. In human umbilical vein endothelial cells (HUVECs), local calcium flickers at the front regulate retraction of lamellipodia and strengthen local adhesion. These calcium pulses were found to activate MLCK and myosin II behind the leading edge and generate force to retract nearby lamellipodia membranes²⁶. The internal, cell-generated traction forces can in turn generate Ca²⁺ flickers mediated by Piezo1 channels³⁹. Piezo1 is one of the SACs expressed in endothelial cells that transduce mechanical stimuli into electrical, osmotic and chemical intracellular signals⁴⁰. Piezo1 channels are located at the plasma membrane and allow cations including Ca²⁺ to enter the cytoplasm on a millisecond time scale once activated by mechanical stimuli. Besides mechanical forces, Piezo1 can also be activated by micromolar concentrations of a small chemical compound Yoda1 that lowers the mechanical threshold for activation⁴¹.

Recent studies in our collaborator Dr. Arnold Ludwig Hayer's group have found that in HUVECs, Piezo1 channels are the main source of calcium flickers. Calcium flickers are enriched at cell-cell junctions in HUVEC monolayers while calcium waves are predominant in subconfluent cell cultures (unpublished observation). The physiological function of calcium flickers and how they propagate inside the cell and binds to downstream calcium-binding proteins remains unclear. In addition, the characterization of the dynamics of calcium flickers such as the rise and decay times are less well-studied. The details about the relationships between calcium

flickers and waves and if flickers originate from waves are not well understood. A better characterization of the dynamics, propagation and evolution of calcium flickers and waves would help us to better understand how Ca²⁺ regulates cellular processes.

2.3 Calcium imaging

2.3.1 Calcium reporter: GCaMP6s

Calcium imaging uses calcium reporters to optically reflect Ca^{2+} status inside the cells. There are two main types of calcium indicators: chemical indicators such as chemical dyes fura-2 and fluo-4, and genetically encoded calcium indicators such as GCaMPs. Fura-2 is a ratiometric fluorescent dye that the maximum fluorescence shifts from 380 nm to 340 nm once binding calcium and the ratio of the fluorescence excited by light of those wavelengths directly reflects the amount of intracellular calcium ions. Fura-2 has a rise time $t_{1/2}$ of 1.4 seconds and a decay time of $t_{1/2}$ 12 seconds⁴², which is slow for calcium flickers but absolute calcium concentrations can be calculated. Fura-2 is also problematic for live imaging because the excitation light is in near ultraviolet and can cause phototoxicity. Fluo-4 is also used to measure cellular Ca^{2+} concentrations in the range of 100 nM to 1 μ M. It has increased fluorescence intensity when compared to Fluo-3 and the acetoxymethyl ester forms are cell-permeable. It is shown that the peak concentration of calcium flickers is typically below 80 nM²⁶, which is lower than the Fluo-4 detection range making it a poor sensor for this application. The rise and decay time t_{20-80} of Fluo-4 are much faster than Fura-2 at 90 ms and 170 ms.

Genetically encoded calcium reporters don't need to be loaded into the cells, instead they are introduced into the cells by various transfection methods and expressed by the cells. GCaMP is a single-fluorescent protein system that consists of a calcium-binding protein calmodulin (CaM), circularly permuted enhanced green fluorescent protein (EGFP) and a calcium-CaM-binding motif M13 from the MCLK. GCaMPs have multiple versions and are the most widely used fluorescent protein-based calcium reporters. The ultrasensitive GCaMP6 developed by *Chen, et. al.* outperforms other sensors⁴³ and has three versions: 6s, 6m, 6f. GCaMP-6s is the most sensitive form but has slower kinetics. GCaMP-6m represents medium kinetics and GCaMP-6f has fast kinetics and shorter rise and decay times. GCaMP-6s is brighter and has a higher signal-to-noise ratio (SNR) compared to -6m and -6f. It has a rise time of 110 ms and decay time of 800 ms. The rise time is similar to Fluo-4 but the decay time is longer, allowing for

a prolonged binding and a more sustained signal. The extended duration of binding to calcium makes it easier to detect subtle changes in calcium levels. However, this can also act as a calcium buffer and impact downstream signaling. Fast kinetics may also introduce variability in the calcium signal because rapid binding to calcium and oscillations between the bound and unbound states is frequent. GCaMP-6s was chosen as the preferred calcium indicator because it offers a balance between binding kinetics, sensitivity and SNR. A GCaMP-6s conjugated with a CAAX motif for targeting to the plasma membrane was used to improve sensitivity to calcium flickers generated by Piezo1 by localizing the sensor to the plasma membrane¹⁹. This is due to the fact that unlike a cytoplasmic sensor, the membrane anchored sensor cannot rapidly diffuse away from the sight of calcium release.

Name	Fura-2	Fluo-4	GCAMP-6s	GCAMP-6m	GCAMP-6f
Туре	Fluorescent Dyes		Fluorescent Proteins		
Rise Time	1.4 s	90 ms	110 ms	90 ms	70 ms
Decay Time	1.2 s	170 ms	800 ms	700 ms	600 ms
Relative Brightness	Data not available		+++	++	++

 Table 1: Summary of the General Properties of some Different Calcium Indicators.

2.3.2 Limit of current calcium imaging methods

Since calcium flickers are transient activities that rise and fall on the time scale of milliseconds, an imaging protocol with high temporal and spatial resolution is needed to achieve accurate identification and characterization. To visualize calcium flickers in live cells, fluorescence microscopy is the method of choice. It involves using fluorescent protein tags or live cell dyes to track the protein or indirectly measure the signal (e.g. ions, phosphorylation) of interest to observe biological phenomena temporally and spatially. In live cell fluorescence imaging, there are a few factors that needs to be considered: sample health, temporal resolution, spatial resolution, SNR⁴⁴. To collect meaningful live cell image data, the main challenge is to achieve an optimal SNR while maintaining a healthy environment for cells to replicate physiological cell dynamics. Cells need to be exposed to adequate light to achieve a good SNR but excess light exposure causes photobleaching⁴⁵ and light-induced cell damage⁴¹. High temporal and spatial resolution are needed to precisely characterize calcium flickers because

some calcium flicker signals can be rapid and thus dim. In addition, if the temporal resolution is lower than the duration of calcium flickers, it may be too slow to capture some flicker activity.

Current calcium flicker imaging and identification protocols developed by Baishali Mukherjee can automatically identify and characterize calcium flicker duration, area and intensity. The protocols were established based on image time series of HUVEC cell monolayers expressing GCaMP-6s where images were captured every second with a 200 ms exposure time for 100 seconds. One aim of this project is to determine if these imaging conditions are sufficient to capture all calcium flickers. It could be that some fast flickers are missed and the 200 ms exposure time may average out some fast flickers with rapid rise and decay times. The aim here is to develop a new method with higher temporal and spatial resolution.

2.3.3 Problems with fast live cell calcium imaging

In fluorescence microscopy, there are multiple factors affecting the image quality including but not limited to: limited spatial resolution, limited signal, uneven illumination, autofluorescence, out-of-focus light and noise. Every image inevitably has noise. There are two major types of noise: shot noise and detector noise⁴⁶. Shot noise is due to the discrete nature of light and the randomness associated with discrete photons arriving at the detector. It is more predominant in low-light conditions and exists in every image. Shot noise usually follows a Poisson distribution, which scales with the pixel intensity. Detector noise is associated with the electronics of the detector and heat (e.g., digital camera readout noise and thermal dark current or photomultiplier tube thermal noise) and often follows a Gaussian distribution and impacts each pixel independently⁴⁷. Here the focus will be on camera-based detectors with shot noise, dark current and readout noise being the main contributors.

On camera-based microscopes, to achieve rapid imaging with high temporal resolution, camera exposure time is reduced to a minimum and camera readout speed is set to a maximum. Reduced exposure time mean that fewer photons are collected by the camera, and the relative contribution from Poisson shot noise and read noise can become significant. Thus, short exposure times lead to a low SNR because of a high level of noise, making it hard to identify objects within images, interpret and quantify biological processes from the image data.

2.4 Calcium Denoising algorithms

2.4.1 Conventional denoising algorithms

Denoising refers to the procedure that aims to remove noise from noisy images while retaining real signal and restore the original images as accurately as possible. It is a fundamental task in image processing. As mentioned above, noise can arise from multiple sources: camera sensing limitations, light conditions and shot noise. The most frequently discussed noises are additive white Gaussian noise, Poisson noise and impulse noise (also known as salt and pepper)⁴⁸. Spatial domain filtering is one of the conventional ways of denoising. It directly estimates each pixel using the information from surrounding pixels. The most popular local filters are the median filter which is effective at removing impulse noise. It picks a window (or kernel) of a certain size (e.g. 3x3) and ranks the pixel values within the window. It takes the median of all the values and assigns the median value to the central pixel in that 3x3 kernel or window. The window is moved iteratively across the entire image. The main disadvantage of this method is that it loses edge information and can impact spatial resolution. There is also 2D Gaussian filter which is based on Gaussian function defined as follows:

$$G(x,y) = \frac{1}{2\pi\sigma^2} e^{-\frac{x^2+y^2}{2\sigma^2}}$$

where x and y represent the coordinate of the pixel and σ decides the extent of smoothing. A larger σ results in more blurring. It first selects a window of a certain size and then redistribute the pixel value based on Gaussian function, giving more weights on the central pixels. The window slides over each pixel of the image. Gaussian filter preserves edge better because the pixels away from the center have less weight. The low pass filters retain signals with a frequency lower than the selected cutoff frequency and attenuates signals with higher frequencies. The lowpass filter can result in blurring and difficulty segmenting features of interest in denoised images. Over the years, more complicated filtering methods such as non-local means⁴⁹, blockmatching 3D⁵⁰ have emerged but simple filtering methods are much more widely used. Most conventional denoising methods using spatial domain filtering impairs the spatial resolution of the original image, making them not an ideal approach to denoise fast calcium flickers videos because it loses the spatial information of the flickers.

2.4.2 Deep learning calcium denoising algorithms

In reality, noise is more complicated and images can have multiple types of noise. It is difficult to apply simple Gaussian or median filter to remove all types of noise, retain resolution and quantitative aspects of images and maintain good quality images. In recent years, deep learning, a subset of machine learning designed to solve more sophisticated problems, has emerged as a powerful tool in multiple fields for multiple applications including denoising ⁵⁰. Compared to conventional denoising algorithms, deep learning algorithms learn from data rather than applying an unchanging mathematical model. The deep learning network gains knowledge about what to expect during iterations of learning, also referred to as content-aware image restoration⁴⁷. Deep learning is highly adaptive to the specific datatype but can also generalize to other similar unseen data. The deep learning denoising algorithms can handle more complex noise patterns and retain and emphasize image features when compared to traditional mathematical denoising methods.

The general principle of deep learning denoising algorithms is to estimate the real intensity for a pixel based on background information. It mimics how we interpret noisy images as humans. For example, there is a high intensity pixel in a region without any labelling and at all other time points it has a value close to zero, then we as humans can recognize this outlier is probably due to a falsely detected photon and is not a true signal. Similarly, if all the surrounding pixels have a high intensity but there is a dark point inside that structure, i.e. nucleus, actin filaments, cell membrane, we can say that is a false negative signal. The convolutional neural network (CNN) is the basic architecture of many deep learning algorithms in image analysis, such as image restoration, deconvolution, image segmentation and classification. It processes images by breaking them into small pieces and recognizes the patterns like edges and structures. It then combines these patterns to learn about more high-level features.

There are two phases in developing a deep learning denoising model: training and testing. Training is to build a model that learns the underlying patterns or features in the data so it can make predictions based on the input data. The model is usually trained on a large dataset, known as the training dataset. The training process typically has three steps: forward propagation, loss calculation, backpropagation. Forward propagation refers to the procedure that the model makes predictions based on input data. Then the difference between the model's predicted values and

the real values is calculated using a loss function, evaluating the performance of the model. The model optimizes its parameters to minimize the loss. The process is then repeated over many iterations, also known as epochs, to minimize the loss and improve the performance.

Testing is to evaluate the model's performance using new, unseen data so that the model can be tested to ensure that it does not overfit with the training data and that it can also be generalized to new inputs. The dataset that has not been seen by the model and is used for testing is called the testing dataset. Based on the results from the test dataset, various evaluation metrics are used to assess the model's performance and accuracy. In some cases, a validation dataset, separate from training and testing dataset but more unbiased, is used to facilitate the training of the model. The loss on the validation set will be small because the model is trained to minimize the loss during validation. The training dataset can be used multiple times while the test dataset is only used once.

There are three main classes of machine learning models: supervised learning, unsupervised learning and reinforcement learning⁵¹. In supervised learning, the model is trained using labeled data pairs. In the case of denoising, the training dataset consists of noisy and low noise image pairs. The low noise images are also referred as ground-truth data. It is named supervised because the model is provided with image pairs and is told one image is noisy and the other image is ground truth and represents what the image should ideally look like. This information is provided by someone so this method is termed supervised. The model then learns to map from the noisy images to low noise images and minimizes the loss functions. Supervised learning is widely used for image classification discriminative tasks. Unsupervised learning, in contrast, uses a training dataset without any labelling. Only noisy images are required to train an unsupervised denoising model. The model learns to find patterns and features without any other external inputs. It is widely used in clustering algorithms and generative tasks. It is more preferrable in live cell imaging because it is often hard to obtain low noise ground truth images. Reinforcement learning learns to make decisions by interacting with the environments. The model receives feedback (rewards or penalties) during training and improves its behavior to maximize cumulative rewards. Supervised and unsupervised learning algorithms have applications in denoising while reinforcement learning is predominantly used in robotics, video games and autonomous vehicles, which is not appropriate for denoising.

Many deep learning based denoising methods have been developed using supervised learning^{52,53} or unsupervised learning⁵⁴⁻⁵⁸. Content-aware image restoration (CARE)⁵² uses image pairs of high SNR and low SNR to train the model based on U-Net architecture with a per-pixel similarity loss. U-Net is primarily designed for biomedical image segmentation with a "Ushaped" architecture and can be recognized a specialized adaption of CNN architecture. U-Net consists of a contracting path containing encoder layers to capture contextual information and an expansive path containing decoders layers that use the information from the contracting path via skip connections. Skip connections connect between layers that skips over one or more intermediate layers to retain the spatial information that might be lost as the image passes through convolutional layers. Noise2Noise⁵⁵ and Noise2Void⁵⁴ are both based on CNNs. Noise2Noise trains on independent pairs of noisy images of the same field of view. The model predicts one noisy image based on the other as input, assuming the images are obtained independently with different random noise but the same structures. Noise2Void takes one step further and it only needs single corrupted data. It estimates the value of a pixel from its surrounding pixels in the same noisy images. Noise2Self⁵⁸ works under the assumption that the noise is statistically independent across different dimensions of the measurement and the true signal has some correlation. It is based on self-supervision, training the denoising model based on single noisy images. DivNoising⁵⁶ is based on fully convolutional variational autoencoders and requires noisy images and a suitable description of the noise distribution. Hierarchical DivNoising (HDN) ⁵⁷ developed by the same team introduces hierarchical Variational Autoencoder architecture and gives the probability distribution of the high SNR images. It generates multiple possible denoised images, allowing users to choose the best one or average them to improve accuracy. The hierarchical structure and probabilistic nature make HDN computationally intensive and hard to set up because there are many parameters that need to be tuned. Among all these models, only CARE is originally designed for fluorescence microscopy images. Most of the denoising algorithms mentioned above are not designed for calcium imaging, so instead of picking those methods, we selected the following denoising algorithms that is adapted for calcium imaging but based on those models.

For deep learning denoising algorithms in calcium imaging, most are based on twophoton calcium imaging of neurons in the intact brain of mice^{59,60}. To our knowledge, there are no existing denoising algorithms that have specifically been developed for endothelial calcium imaging. Two photon calcium imaging in neurons also suffer from low SNR problems because images are collected deep in brain tissue, up to 500 μ m below the cortical surface⁶⁰ and a lot of fluorescence signal is lost due to scattering within the tissue. As mentioned aforehand, calcium ions activate the release of neurotransmitter at synapses and are essential for the propagation of electrical signals. Most neurons have an intracellular calcium concentration of about 50–100 nM at rest. The calcium level can increase 10 to 100 times above baseline in the event of electrical activity⁶¹. The peak calcium concentrations in calcium activity in neurons is much higher than the peak calcium level of calcium flickers in HUVECs (~80 nM)²⁶. Also, the focus of calcium imaging in the brain is on high temporal resolution to monitor fast calcium dynamics on a few hundreds of millisecond timescale⁶². In endothelial cells, spatial resolution is also important because calcium signals are not physically localized within small neuronal structures or synapses and it is required to reveal how calcium flickers propagate as calcium waves. Since deep learning denoising algorithms are generalizable and can be retrained with similar datasets and adapted to specific datatype, it is possible to apply current promising calcium denoising algorithms to low SNR calcium images of calcium flickers in HUVEC monolayers.

For this study, we selected three of the most commonly used state-of-the-art calcium denoising algorithms: Neuro Imaging via Deep Learning (NIDDL)⁵³, Deep Interpolation⁶⁰ and DeepCAD⁵⁹. Each of them is based on a different deep learning model and all of them show satisfactory results when applied to low SNR laser scanning confocal or two-photon microscopy images of calcium signals in images of neurons.

2.4.3 Neuro Imaging via Deep Learning (NIDDL)

Neuro Imaging via Deep Learning is a supervised denoising method trained with whole-brain data, ventral coed neurons data and neurite structures in *C. elegans* imaged using a Bruker Opterra II Swept field confocal microscope with an EMCCD camera⁵³. It requires only a small set of training image pairs (~500) acquired independently and can be non-temporally sequential, making it easier to acquire the training data because images can be acquired from fixed samples at different times. The general principle of NIDDL is to train the network to predict high SNR image stacks given low SNR (can be low laser-power or short exposure time) image stacks (Fig. 2). Subsequently, in the testing phase, trained models are applied to denoise video data by independently denoising each volume in the video. It optimizes CNN by using a 20-30x smaller

memory footprint and is about 3 times faster in training and testing than other similar algorithms. NIDDL is flexible, users can choose and test many parameters based on the dataset including the training mode and the loss function. The training mode is one of three types, the 2D, 2.5D, or 3D mode. The 2D mode is used when the input and output are 2D images. The 2.5D mode is used when the input is a 3D stack consisting of z-plane above and below the in-focus image to be denoised and the output is the designated denoised image from the middle of the stack. For 3D mode, both the input and the output are 3D stacks. The loss function is one of two types, L1 loss or L2 loss. L1 loss, also known as mean absolute error, is the sum of the absolute differences between the predicted

and actual image intensity values. L2 loss, referred to as least squares error or mean squared error when averaged over a dataset, is defined as the sum of squared differences between the predicted and actual image intensity values. NIDDL has been implemented in the open-source software platform napari (https://napari.org/) with pretrained models using multiple datatypes (e.g. whole brain, ventral cord, neurite, synthetic

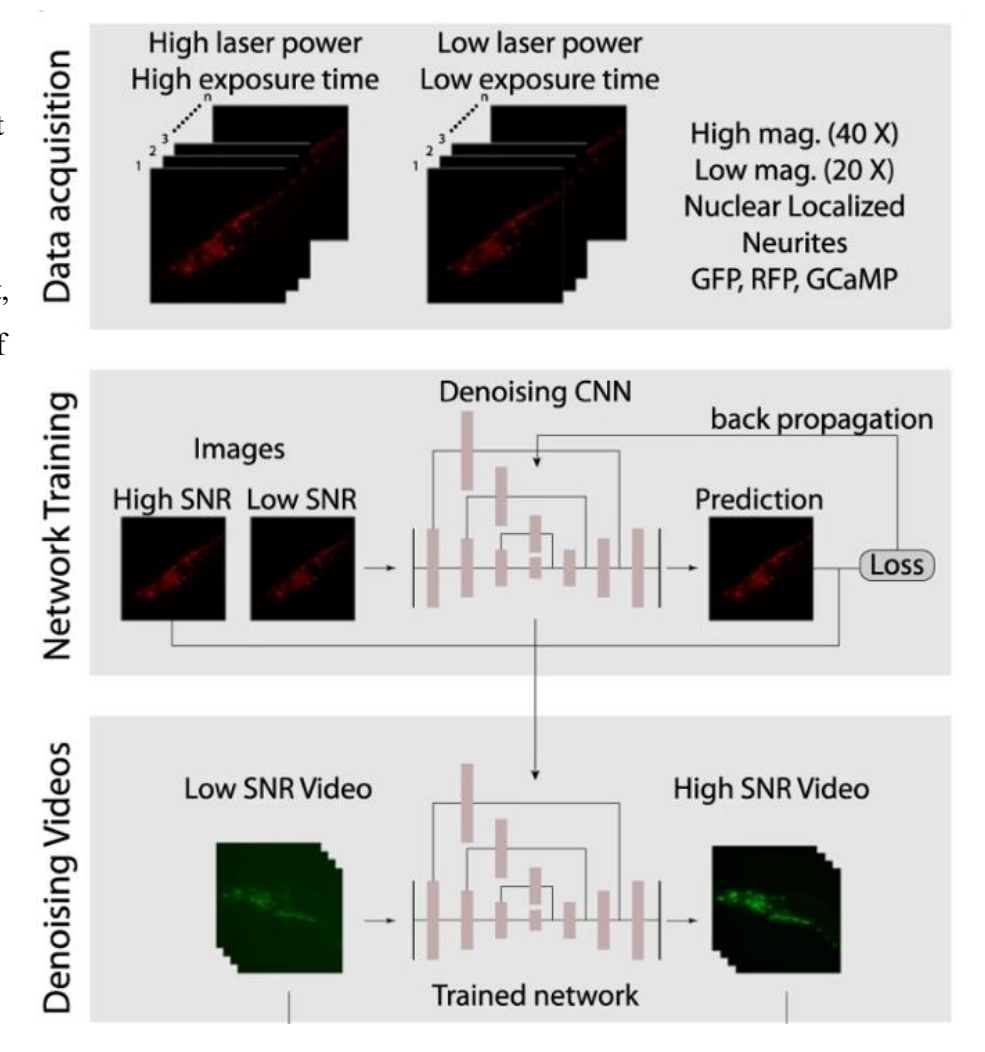


Figure 2: The architecture of NIDDL. Reused with permission from Creative Commons license (https://creativecommons.org/licenses/by/4.0/): Nature Communications, Fast, efficient, and accurate neuro-imaging denoising via supervised deep learning, Shivesh Chaudhary et al., 2022

images). Napari is a Python library for n-dimensional image visualization, annotation, and analysis.

Compared to unsupervised methods, supervised methods are expected to achieve higher accuracy and should be more generalizable. But there are a limited number of supervised denoising methods because it is often difficult to acquire ground-truth data. In calcium imaging, not all microscopes can collect high SNR and low SNR videos simultaneously. If the unsupervised method is trained with non-temporally linked data, it is not clear if temporal structural features can be preserved from independently denoised images.

2.4.4 DeepInterpolation

DeepInterpolation is an unsupervised denoising method that was trained using low SNR two-photon calcium data with GCaMP-6f as the calcium reporter⁶⁰. The images were obtained in visual or somatosensory cortex in brains using live or anesthetized mice⁶³. It can also be applied to functional magnetic resonance imaging (fMRI) image datasets and extracellular electrophysiology recordings. DeepInterpolation uses a low SNR image to predict a high SNR image. It enhances SNR by up to 15-fold and is able to identify and segment up to 6 times more neuronal features in two-photon image datasets. For extracellular electrophysiology recordings, it detects up to 25% more spiking events and with fMRI image datasets there is a 1.6-fold increase in SNR. In neurons, it is hard to image pairs of sample images with identical signals but different

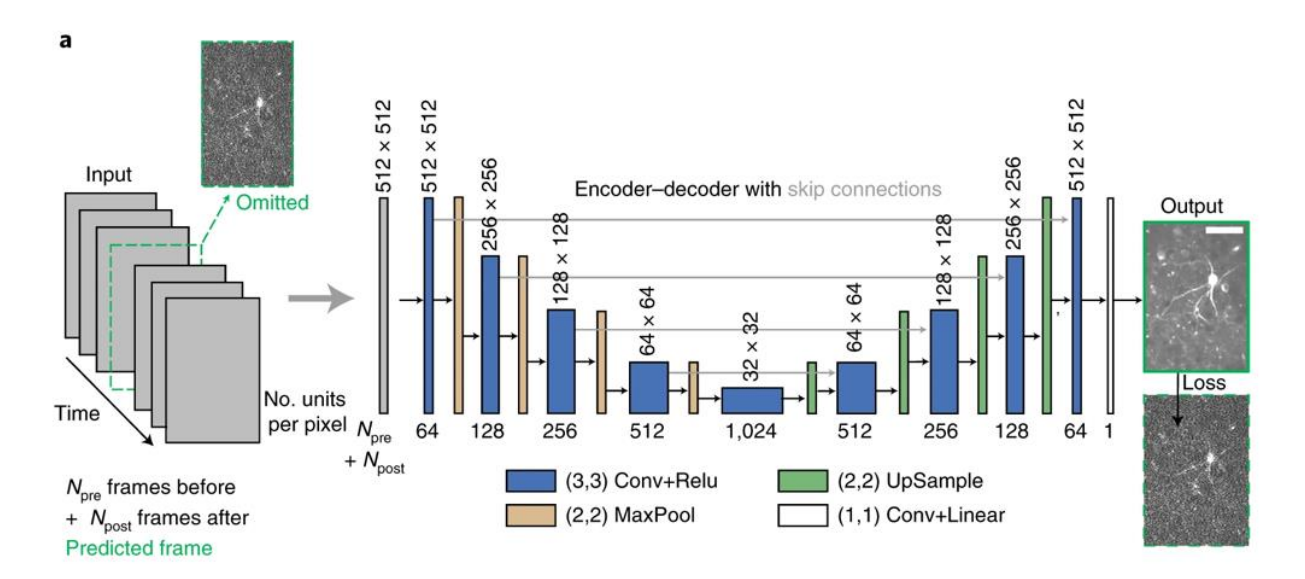


Figure 3: The architecture of Deep Interpolation. Reused with permission from Springer Nature: Nature Methods, Removing independent noise in systems neuroscience data using DeepInterpolation, Jérôme Lecoq et al., 2021.

noise (Noise2Noise) because the dynamics are so rapid. Therefore, DeepInterpolation adopts an approach based on the Noise2Self and Noise2Void frameworks. It learns the spatiotemporal relationship between each data point and its spatial and temporal neighbours to minimize the reconstruction loss function. The architecture of DeepInterpolation is based on a UNet-inspired architecture and follows the two principles (Fig. 3): a single pixel shares information or is correlated with surrounding pixels within a fixed local region; based on the decay dynamics of GCaMP-6f, frames up to 1s away from the target frame may carry useful information. During training, one frame is omitted, and the network learns to predict the omitted frame using the information from its neighboring frames in time, i.e., 10 frames before and after the omitted frame. DeepInterpolation must work under the theory that the noise present in the target sample image is independent from adjacent sample images, otherwise it may lead to overfitting. The framework eliminates overfitting by omitting the target image frame only once, therefore there are no iterations over the whole dataset that would require huge datasets ($\sim 10,000$ image frames). Since the training image dataset is large, it is computationally demanding. For all three datatypes, training on a single GPU can take 2-3 days with continuous processing. L1 loss was used for both two-photon imaging and fMRI image datasets and L2 loss was used for electrophysiological datasets.

2.4.5 DeepCAD

DeepCAD is a self-supervised deep learning denoising method that enhances the spatiotemporal resolution of images by more than tenfold⁵⁹. It is based on the Noise2Noise denoising method. DeepCAD works under the assumption that a deep neural network can converge to a mean estimator even it is trained using another corrupted image of the same scene and the optimal network parameters are similar to those trained with ground truth images⁵⁵. It separates a time lapse video into two sub-stacks consisting of interlaced frames from the input image dataset and then trains the model to predict one stack from the other (Fig. 4). DeepCAD requires a high imaging rate (~30 Hz) so that two consecutive frames have essentially the same structures but different noise patterns and can be considered as two independent images of the sample. The two sub-stacks are corresponding and the corresponding image frames have the same structure but different noise, so the network can learn what structures to expect despite the random noise. The minimum data required to achieve satisfactory denoising results is a single low SNR video of 3,500 image frames. A higher image sampling rate and more training frames

can lead to better performance. The original algorithm was trained with images of calcium spikes in the brains of live mice activated by action potentials in neurons using transgenic mice (Ai148D/Rasgrf2dCre) imaged with a two-photon laser scanning microscope. DeepCAD deploys a 3D U-Net that uses the spatiotemporal

correlation of calcium

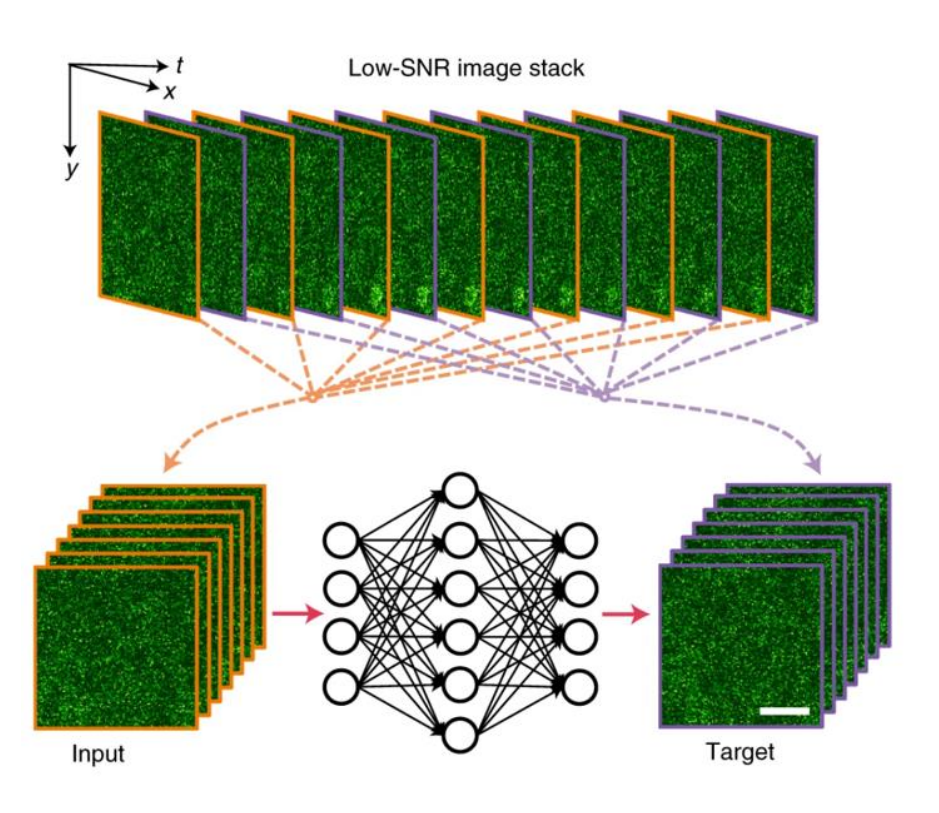


Figure 4: Architecture of DeepCAD. Reused with permission from Springer Nature: Nature Methods, Reinforcing neuron extraction and spike inference in calcium imaging using deep self-supervised denoising, Xinyang Li et al, 2021.

images and it is composed of a 3D encoder module, a 3D decoder module and three skip connections. Regarding the loss functions, the average of a L1-norm loss and a L2-norm loss term were used. DeepCAD also reinforces the accuracy of neuron extraction and segmentation. Recently, the new real-time version (DeepCAD-RT) was developed for real-time denoising⁶⁴ and it has been implemented as a Fiji plugin with pretrained models. Since imaging systems, experimental conditions, model systems (e.g. whole brain, brain slices, isolated neurons) cell types and morphology (e.g. large, rounded cells versus elongated branching neurons) all vary in different research projects, it is highly recommended to train a customized DeepCAD model using experiment specified image data for optimal performance. It should be noted that the training of a customized model is computationally demanding and needs to be implemented using TensorFlow packages, which requires the users to have some coding background.

3 Methodology

3.1 Cell Culture

hTERT-immortalized HUVECs (HT73)⁶⁵, were cultured in Endothelial Cell Growth Medium 2 (PromoCell, Cat# C-22011), supplemented with hygromycin B (InvivoGen, Cat# ant-hg-1) at a working concentration of 10 μ g/ml and blasticidin at a working concentration of 50 μ g/ml (InvivoGen, Cat# ant-bl-1) to maintain expression of transduced products (hTERT). HT73 cells transfected with GCaMP6s-CAAX¹⁹ to report cytosolic Ca²⁺ levels at the plasma membrane were provided by Dr. Hayer's laboratory.

3.2 Preparation of imaging slides

Glass bottom 8-well imaging slides (Ibidi, Cat# 80827) were coated with 3.2 mg/ml type I collagen solution (Advanced BioMatrix, Cat# 5005) diluted 1:100 in phosphate buffered saline (PBS) (Gibco, Cat# 10010-023/10010-049) at 37°C with 5% CO₂ for 4-24 hours before use. Cells were cultured to maintain an 80% confluency in 60-mm dishes before subculturing. Cells were washed with PBS before adding 1 mL of 0.05% trypsin-EDTA (Gibco, Cat# 25300-054). Trypsin was aspirated after 2 minutes, leaving only a thin layer at the cell dish. The plate was incubated for 2 minutes at 37°C with 5% CO₂. Cells were resuspended with 4-5 ml medium to neutralize the trypsin and 10 µL of the solution was used for cell counting. Approximately 20,000 cells in 200 µL cell growth medium were plated in each well of the imaging slides and were kept at 37°C overnight to form a uniform monolayer. On the following day, the medium in each well was replaced with 200 µL Live-cell Imaging Solution (LIS). The LIS solution was prepared with 125 mM NaCl, 5 mM KCl, 20 mM HEPES solution (pH 7.4), 1.5 mM MgCl₂, 1.5 mM CaCl₂, 10 mM D-glucose, 1% fetal bovine serum (Fisher Scientific, Cat# 35077CV) and 5 ng/ml basic fibroblast growth factor (Cedarlane Labs, Cat# CL104-02-50UG). The plate was left to settle in the microscope mounted live cell environmental control chamber (Live Cell Instrument, Cat# CU-501) for about 10 minutes to stabilize the cells at 37°C and 5% CO₂. Right before imaging, 100 µL LIS solution supplemented with Yoda 1 (Sigma-Aldrich, Cat# SML1558) at a working concentration of 0.1 μ M was added to each well.

3.3 Cell fixation

The cells were fixed after live cell imaging in order to collect identical image pairs with fixed cells. The volume of each well was first reduced to $100 \mu L$. Then $100 \mu L$ of 16% paraformaldehyde (Electron Microscopy Sciences, 15710) diluted 1:3 in PBS was added for 15 minutes at 37°C. Cells were immersed in PBS for 5 minutes and then washed three times with PBS. The fixed plate was stored in PBS with 2% sodium azide in the 4°C fridge for up to three weeks.

3.4 Setup of Widefield Calcium Imaging

Widefield imaging was accomplished using a Leica DM1600B microscope (Leica Microsystems) with a Leica HC Plan Apochromat 20x/0.7 NA objective lens. The illumination was provided with an X-Cite 120 LED (370-700nm, 100 W) light source. The emitted fluorescence passed through an EGFP filter cube with an ET470/40x excitation filter, T495lpxr dichroic mirror and an ET 525/50m emission filter and was imaged with a digital scientific CMOS camera (C13440-20CU, Hamamatsu, Japan). This microscope is part of a Total Internal Reflection Fluorescence (TIRF) system but all controls for TIRF were disabled including the laser excitation and only the widefield imaging stand was used for all experiments. MetaMorph (Molecular Devices Inc., Version 7.10.5.476) software interface was used to achieve stream acquisition with minimum delays. Pixel size was 0.401 μm when the 20x objective was used.

3.5 Calcium Imaging Experiments

Live cells and fixed cells were imaged with the same conditions. Before each imaging session the fluorescence lamp intensity was measured using the 20x/0.7 NA objective lens and a laser power meter (Coherent FieldMax II, 1098579) and was maintained at ~175-180 μ W as the baseline lamp intensity for low SNR images. Stream acquisition was used to collect images continuously with minimum delay. The MetaMorph software keeps delays between frames of stream acquisition at a minimum of ~1 ms over ~200 images. Time lapse datasets of low SNR ratio images were captured at 20 ms, 10 ms or 5 ms exposure times, 20% lamp intensity (~175-180 μ W) with 2x2 pixel binning. More images were captured with shorter exposure time experiments to ensure the total experiment duration was constant. For example, the videos captured at 20 ms exposure time had 200 image frames while the videos captured at 10 ms exposure time had 400 image frames. High SNR ratio image datasets were captured at 200 ms

exposure time with no delay, 20% lamp intensity with 2x2 pixel binning. The high SNR and low SNR image stacks were captured of the same field-of-view (FOV) to compare the frequency of calcium flickers for the same cells but were not synchronous (the time interval between two stacks were ~20 s). For the fixed cell image pairs, they were imaged at the same FOV at 20 ms or 200 ms exposure time. At the end of the imaging sessions, the cell slide was removed, and a time lapse video of background and noise was captured and used to correct for black "dead" and saturated "hot" camera pixel artifacts and camera noise, keeping all other parameters the same.

To evaluate the influence of lamp intensity and potential phototoxicity on the number of calcium flickers, timelapse videos were captured at 200 ms exposure time. The lamp intensity was variable among experiments. The same baseline intensity (\sim 175-180 μ W) was used. Then images were taken by doubling and tripling the lamp intensity until it reached 100%. For example, the baseline intensity was at 25%, then images were captured using 50%, 75% and 100% lamp power.

3.6 Model training

Since the training procedure of the deep learning methods is often computationally demanding and requires graphics processing units (GPUs) to accelerate the training, all the trainings were done remotely through the cloud platform Digital Research Alliance of Canada (DRAC) (previously known as Compute Canada, https://alliancecan.ca/en) or Google Colab. The general procedure to train a published deep learning method is: 1. Download the whole repository to the cloud service. 2. Install the virtual environment on the cloud service. 3. Train a new model with a new dataset. 4. If needed, adjust the code or parameters to achieve better performance.

3.6.1 NIDDL

There are two versions of NIDDL: one was implemented using TensorFlow and the other was implement using pytorch. The version using TensorFlow was outdated and could not be installed on the cloud service so the pytorch version was used. The training of NIDDL was completed on the cloud platform DRAC. The training dataset was composed of 524 matched image pairs of high SNR and low SNR images. To ensure matched pairs, the cells were fixed before imaging and the same field of view was imaged with different conditions. The high SNR images were captured with a 200 ms exposure time and the low SNR images were captured with

a 20 ms exposure time. Each image (1024x1024) was cropped to generate four sub stacks (512x512) to match the original network design to operate with images of 512x512 pixels. The basic model used is UNet fixed. The architecture is the same as UNet, which has 4 downsampling layers with non-linear activation (ReLU) and 4 up-sampling layers (Fig. 2). The first feature map is 512x512x32 and the depth of the feature maps doubled after each down-sampling layer and reduced to half after each up-sampling layer. UNet fixed has a fixed depth of all feature maps of 32 compared to UNet which has a varying depth (it begins with 32 channels and doubles after each down-sampling and halves after each up-sampling), reducing the model size and decreasing the training and testing time⁵³. There are also other architectures to select from that were tested: UNet, hourglass wores, hourglass wres. Based on the original dataset, UNet fixed and hourglass wres achieved higher accuracy and required smaller memory footprint compared to hourglass wores. For our datasets, UNet fixed outperformed Hourglass wres so this was chosen moving forward. Adam optimizer⁶⁶ was used for training with a learning rate of 0.001, which is a key hyperparameter that determines how much the model's parameters are adjusted at each step. The model uses a 2D model and L1 loss is used. The model was trained for 500 epochs using one GPU (Nvidia V100SXM2, 16G memory) and took about 1 hour (Refer to the table here).

3.6.2 Deep Interpolation

The training of Deep Interpolation was performed on Google Colab because the version of TensorFlow required was incompatible with DRAC. The denoising network is designed to train on a single input dataset because the original training dataset is one single or multiple continuous videos. So, one low SNR video of 1000 image frames captured with a 20 ms exposure time was used to train the denoising neural networks. The video was cropped to 512x512 pixels for compatibility with the model. The architecture of the model is also based on UNet, with a learning rate of 0.0001. The model consists of 3x3 2D convolutional layers followed by rectified linear activation function (ReLU), 2x2 max pooling (down sampling) layers and 2x2 up sampling layers (Fig. 3). The L1 loss function was used. Temporal information was collected using 10 frames before and after the target frames. The model was trained for 19 epochs using a high-RAM 16GB T4 GPU (Tesla 4) and it took 4 hours to complete the training.

3.6.3 **DeepCAD**

The training of DeepCAD was conducted on the cloud platform of DRAC. The training dataset of DeepCAD consisted of 20 low SNR videos from two independent experiments. Each video was made up of 1024x1024 pixel 1000 image frames collected with a 20 ms exposure time. The 3D encoder has three encoder blocks and each block consists of two 3x3x3 convolutional layers, followed by a leaky rectified linear unit (LeakyReLU) and a 2x2x2 max pooling layer. There are three decoder blocks in the decoder module: two 3x3x3 convolutional layers followed by LeakyReLU and a 3D nearest interpolation. Adam optimizer⁶⁶ was used for training with an initial learning rate of 0.00005 and exponential decay rates of 0.500 for the first moment (beta1) and 0.999 for the second moment (beta2). The number of feature maps is 16. The width and height of 3D patches is 150 and the time dimension of 3D patches is 150. The overlap factor between two adjacent patches is 0.25. The model was trained using one GPU (Nvidia V100SXM2, 16G memory) for 20 epochs and took about 18 hours to complete the training. Training time could be shortened with a more powerful GPU or parallel computing using multiple GPUs. Multiple trainings were done with different datasets (first trained with 10-15 low SNR videos) and fewer epochs. The model trained with 20 videos and 20 epochs achieved good performance based on the loss function and manual inspection of the images.

3.7 Model testing

All the testing of the three denoising models were performed on DRAC platform but it could be done locally on a personal laptop if needed. The same testing datasets were used for all three models so that the results were comparable across different models. The testing dataset was separate from the training dataset. It was composed of 30 low SNR videos imaged with a 20 ms exposure time from three independent experiments (10 videos per experiment). Each video had 200 frames and all test images were preprocessed to remove camera noise. Camera noise reduction was done by subtracting the averaged image of a time lapse image data series captured without any sample on the microscope. Since some denoising models work with 512x512 image size while the original images obtained on the microscope are 1024x1024, all result images with the size of 512x512 were concatenated with other sub stacks from the same original video to the uniform size of 1024x1024. All the output time lapses images are in 32-bit.

3.7.1 NIDDL

The general testing procedure of NIDDL consists of the following steps: 1) Crop the original 1024x1024 testing dataset to generate four 512x512 sub stacks and convert the video stacks to 8-bit. 2) Feed the images into the pretrained model. 3) Recombine the sub stacks to generate 1024x1024 images. 4. Convert the individual images to video stacks. The testing time was fast and only took about 1 minute per video of 200 frames, but the preprocessing and postprocessing work was tedious.

3.7.2 Deep Interpolation

Similar to NIDDL, deep interpolation also needs to streamline the image size. The testing procedure was as follow: 1) Crop the testing dataset to 512x512 and convert to 8-bit. 2) Feed the videos into the pretrained model. 3) Convert the output videos from h5 to tiff files. 4) Combine the substacks (top right, top left, bottom right, bottom left) into one video of size 1024x1024. The testing time was about 2-3 minutes for each video.

3.7.3 **DeepCAD**

The testing phase of DeepCAD was straight forward: 1) Convert the testing dataset to 8-bit. 2) Use the pretrained model to generate denoised videos. It took about 3 minutes to generate each denoised video.

Model	NIDDL	Deep Interpolation	DeepCAD
Difficulty to set up	+++	+++++	+
Computationally demanding	+	+++++	+++
Training time	+	+++++	++++
Testing time	+	+	+
Test image Output Format	512x512, .tiff	512x512, .h5	1024x1024, .tiff

Table 2: Comparison on difficulty of usage and time required for training and testing among selected denoising algorithms.

3.8 Quantification Methods

3.8.1 Generation of pseudo high exposure time videos

To validate the denoising results, pseudo high exposure time videos were generated by summing together n consecutive frames to mimic video images captured with longer exposure

times. For example, 10 sequential image frames in a video imaged with a 20 ms exposure time were added together to generate 1 image frame imaged with a pseudo 200 ms exposure time. At the same time, using this method resulted in the total number of image frames being reduced by ten-fold.

3.8.2 Analysis of the intensity plot

The measurement of intensity along a straight line was done using ImageJ/Fiji software. The frame of interest was first selected. Then the same frame from three different denoised models were extracted from the original video and combined as a stack. A straight line was drawn across the area of interest using the straight-line drawing tool, and measurements of the intensity along the same line were taken using *Analyze->Plot Profile*, which generates a plot of the intensity over distance (in pixels). The plot from different denoising results were normalized to 0-255. To plot the flicker intensity change over time, an area of interest was selected with *Freehand Selections* and the following steps were taken to plot the mean intensity change over time: *Image->Stacks->Plot Z-axis Profile*.

To plot the histogram of the pixel intensity in Deep Interpolation denoised video images, the *Analyze->Histogram* feature in ImageJ/Fiji was used to analyze the distribution of pixel intensities.

3.8.3 Manual counting the number of calcium flickers

The number of flickers was manually counted by eye to validate the denoising results. If the image size was 1024x1024, it was cropped to four 512x512 sub stacks for the convenience of counting. The counting was done manually by watching the time-lapse image stacks multiple times to avoid missing flickers. Calcium flickers were identified as localized transient calcium activity that occurred mostly at cell-cell junctions. The change of intensity in calcium signals was checked to make sure the flicker activity was dynamic and if so, it was counted. If the calcium signal diffuses to more than 1/4 size of the cell, it was recognized as a calcium wave and not counted. If there was a constantly bright object present in the majority of the image series, it was considered as an artifact, perhaps a stationary piece of debris. Similarly, if it was a moving bright object, it probably was a piece of debris, and it was not counted.

3.8.4 Automated detection of calcium flickers in denoised videos

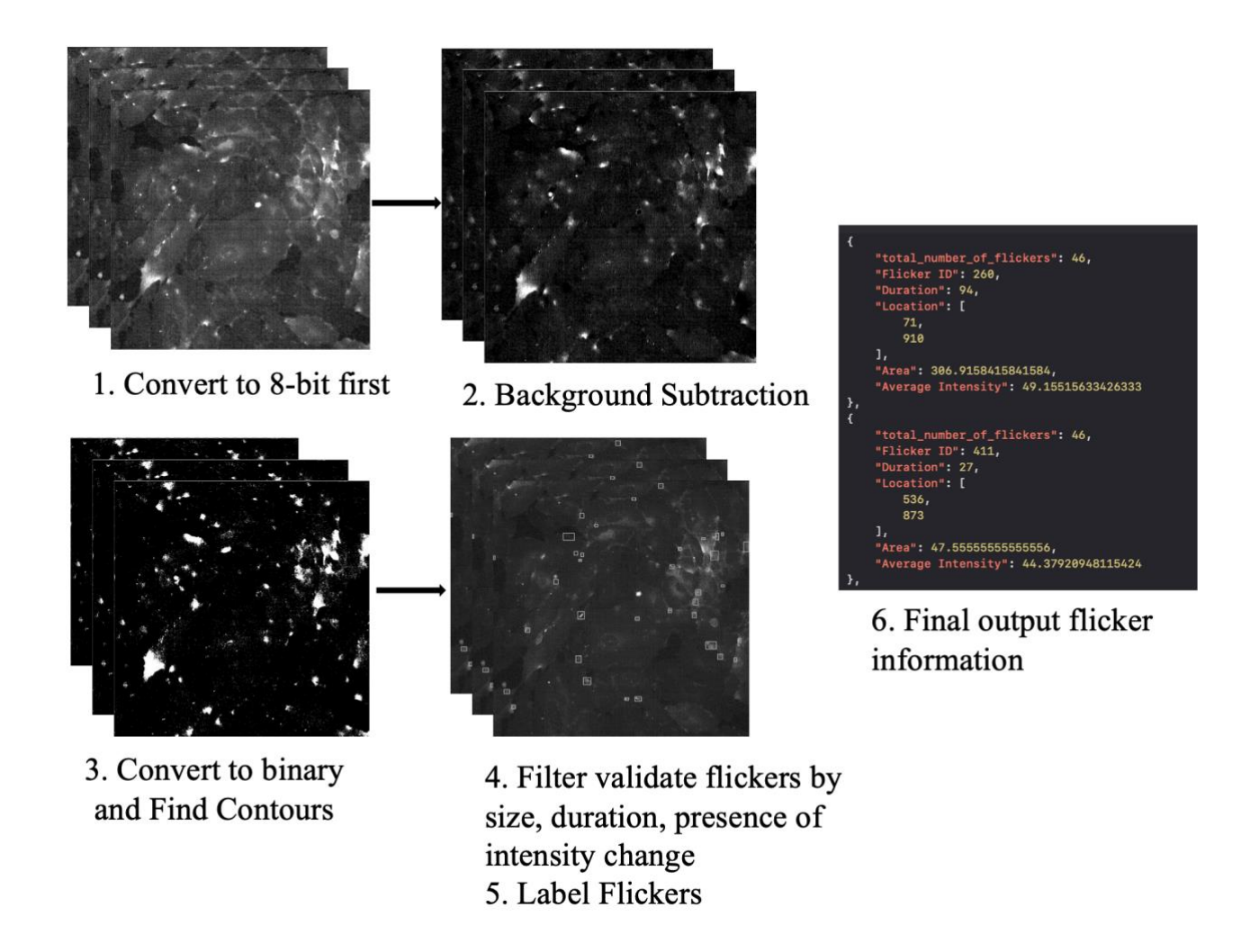


Figure 5: Illustration of automated detection of calcium flickers.

In order to better characterize the calcium flicker, automated detection of calcium flickers was developed to measure the duration, average intensity and area of flicker activity. The automated detection in denoised image videos or in high SNR conditions was achieved using the following steps (Fig. 5): 1) Convert to 8-bit images. 2) Subtract the background information (e.g., autofluorescence, cell shape) by taking the average of the whole image video stack and subtracting it from each image frame. 3) Convert the corrected image stacks to a stack of binary images and find the contours of calcium flickers from the binary images using the *OpenCV* library⁶⁷. 4) Use the *OpenCV* library to detect the contours of calcium flickers and detected flickers were then filtered by adjusting the size/duration of flickers, intensity threshold, minimum neighbor flicker distance to ensure only "real" flickers of interest were identified in the corrected

images. The intensity threshold was fine-tuned according to different imaging conditions. Other parameters used to detect calcium flickers were as follows: min_size = $3.2 \ \mu m^2$ (20 pixel²), max_size = $160 \ \mu m^2$ (1000 pixel²), min_duration = 1 frame, max_duration = total number of frames, minimum distance between neighbouring flickers = $4 \ \mu m$ (10 pixels). 5) Validated flickers were labelled and a rectangle was drawn around the validated flicker for better visualization. 6) The output .json file was created and exported and contained information about all the detected flickers including the total number, duration, location, area and average intensity. The script was implemented using Python. For denoised data, it reached an accuracy of about 92% and for raw data, the accuracy was about 78%.

3.8.5 Calculation of SNR

The SNR was defined as the ratio of signal to noise. For this study, we calculated the SNR for each detected calcium flicker by taking the maximum intensity of the flicker divided by the standard deviation of the intensities for the entire duration when the flicker was active. We first used the automated detection script to identify calcium flickers, and then extract the location information for each flicker. Within the flicker region, the SNR was calculated by taking the intensities from the original video stack. The SNR of each video stack was the average SNR of all detected calcium flickers. This reflects the SNR more accurately because we were interested in the noise present in calcium signals, rather than the shot noise in the background signals that do not have calcium activity. The two tailed, equal variance, pairwise T-test was used as a statistical approach to evaluate the significance of difference between dataset pairs.

3.8.6 Generation of simulated calcium data

Simulated calcium data was generated by adding Poisson and Gaussian noise to the 200 ms exposure time high SNR videos. The Poisson noise was generated using NumPy library⁶⁸ with a scaling factor of 30 and the Gaussian noise was generated with a standard deviation of 15 times the mean intensity of the original video images.

The performance of denoised models was evaluated by determining if the detected flickers in denoised results overlapped in time with the original 200 ms exposure time data. Automated flicker detection as described in Sec 3.8.4 was used. The start and end frame of each detected flicker in the denoised results were compared to the same detected flicker in the original 200 ms exposure time videos. Flickers were, identified by mapping the x,y information of the

flickers, with a tolerance of \pm 2 frames. Precision value was reported as the fraction of true positive detected flickers among all the detected flickers, reflecting the accuracy of the algorithms. Recall value was defined as the fraction of true positive detected flickers among all detected flickers in the original 200 ms exposure time image data, indicating how many 'real' flickers were retrieved.

4 Results

4.1 Deep learning denoising algorithms enhance image SNR better than traditional methods

Calcium flickers were imaged with a higher temporal resolution by setting the exposure time to 20 ms. This is 10x faster than previous conditions where the SNR was optimized with a 200 ms exposure time (Fig. 6A). Calcium images collected with a 20 ms exposure time were noisier and it was difficult to distinguish calcium flickers from background (Fig. 6B). Several methods including mathematical and deep learning denoising approaches were selected to enhance the SNR and generate images that were more representative of "true" calcium signals.

As mentioned in the introduction section, three different types of deep learning calcium denoising algorithms were selected and their characteristics are summarized in Table 3.

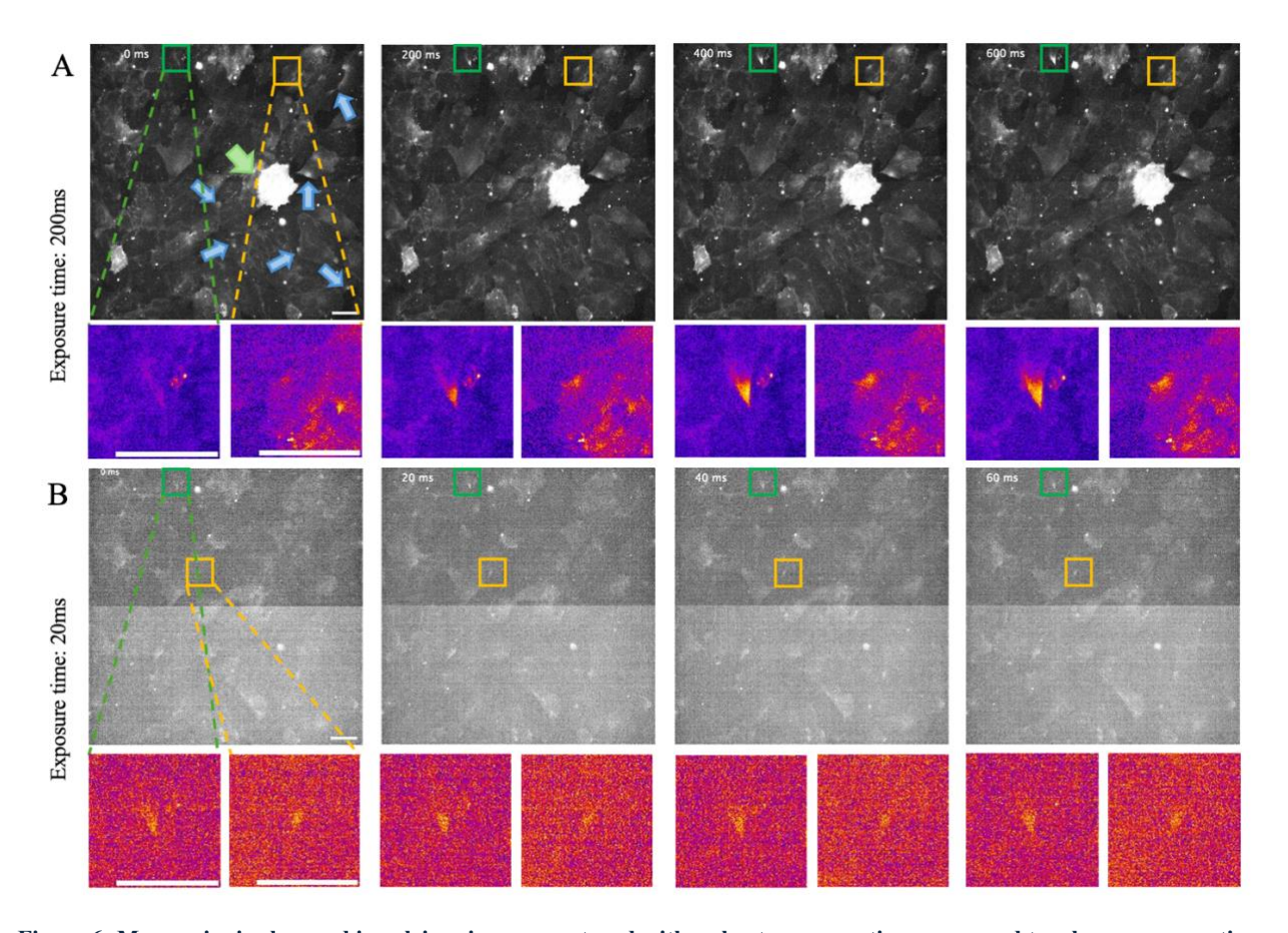


Figure 6: More noise is observed in calcium images captured with a short exposure time compared to a long exposure time. Representative widefield images of HUVEC monolayers treated with Yoda 1 imaged with different exposure times imaging conditions. The green arrow points toward a calcium wave and the blue arrows point towards calcium flickers. The lower panel are zoom-in versions of the green/yellow square boxes. (A) Images were obtained with a 200 ms exposure time, 5 fps and 20% lamp intensity. (B) Images were obtained with a 20 ms exposure time, 50 fps and 20% lamp intensity. The images are of the same field of view at different time points. Brightness and contrast were auto adjusted for better visualization purposes. Image size: 1024x1024. Scale bar: $40 \mu m$.

NIDDL ⁵³ (2022)	DeepInterpolation ⁶⁰ (2021)	DeepCAD ⁵⁹ (2021)	
Based on confocal images of the mouse brain Supervised	Based on two-photon images of the mouse brain Unsupervised		
 512x512 Higher accuracy and generalizable Requires ground-truth data (supervised) A relatively small training datasets (~500 image pairs) is needed 	 512x512 Adapts from Noise2Self and Noise2Void models Increase SNR by 15-fold Takes temporal information from pre and post frames Trained on a huge dataset ~10,000 frames 	 1024x1024 Based on Noise2Noise model Increase SNR by 10-fold A training dataset of ~3500 frames with high-speed imaging is needed 	

Table 3: Three selected deep learning calcium denoising algorithms and a summary of their different characteristics.

The algorithms were only trained with low SNR 20 ms exposure time calcium images and tested with a different set of calcium images. Each calcium flicker is unique, and it is not possible to set up the microscope to image simultaneously at a shorter and longer exposure time in live cells. Also, since two of the denoising algorithms are unsupervised and do not require ground-truth data, it is difficult to validate the results. To overcome these issues 10 consecutive image frames were added together to generate pseudo 200 ms long exposure time. This also meant that the test data was composed of exactly the same images as for the raw data and all denoising approaches including the representative traditional mathematical denoising approaches of Gaussian and median filtering.

The rolling shutter feature of the scientific CMOS (sCMOS) sensor scans the image from the center to the top or the bottom, resulting in slightly different noise and background properties within the two halves of the images and a horizontal line in the middle of the image (Fig. 7A). In addition, uneven illumination was more obvious in shorter exposure time images (Fig. 7A). To remove the background, uneven illumination and fixed the camera pattern, the test images were preprocessed by subtracting a camera correction image collected with the same conditions but with no sample on the microscope and no lamp illumination (Fig. 7A).

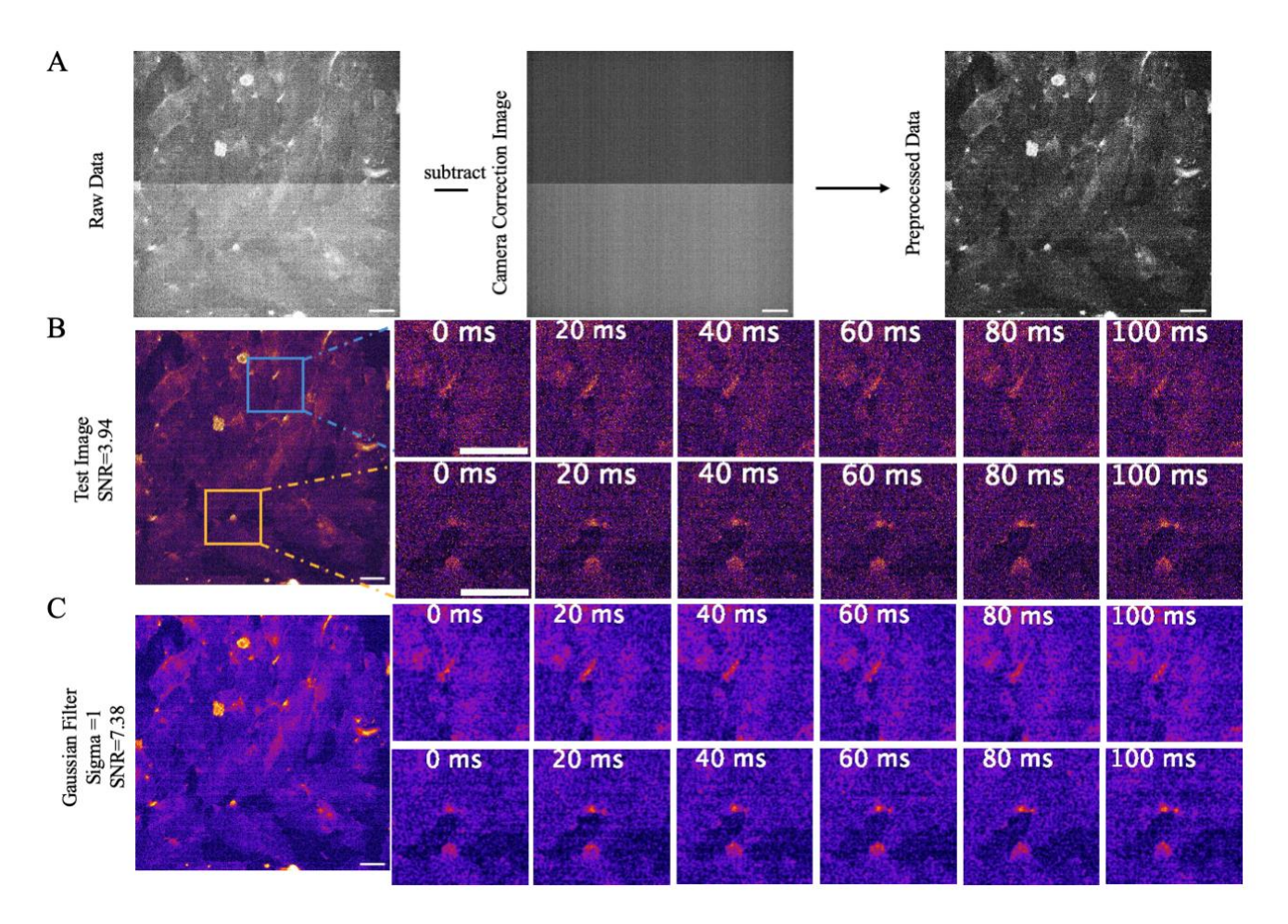


Figure 7: Median filter improves SNR in noisy images. Representative test images with HUVEC monolayers treated with Yoda1. (A)Test images were preprocessed by subtracting a camera correction image to eliminate the fixed pattern artifact from the rolling shutter (horizontal line in the middle of the image). (B) Time lapse images of the test data. The images were captured with a 20ms exposure time, 50 fps, 20% lamp intensity. The right panels represent zoomed-in regions of interest from the time series images shown in the yellow and blue boxes. (C) Denoised test images with the application of a Gaussian filter with a sigma of 1, which corresponds to a 3x3 kernel. The right panels are zoomed-in versions of the same areas at the same time points in B. Brightness and contrast were auto adjusted for better visualization purposes. Image size: 1024x1024. Scale bar: $40 \mu m$.

By applying different denoising methods, the SNR was improved to a different extent (Fig. 7, 8) when compared to the raw test image data (Fig. 7B). The Gaussian filter (Fig. 7C) and median filter (Fig. 8A) removed noise, but the resulting images are slightly blurred. The background was reduced but the images were still somewhat pixelated (Fig. 7, 8).

The NIDDL deep learning algorithm corrupted the test image, key features in the data disappeared and black rectangular blocks were randomly introduced after image processing (Fig. 8B). SNR was not calculated for NIDDL denoising results because this was not meaningful

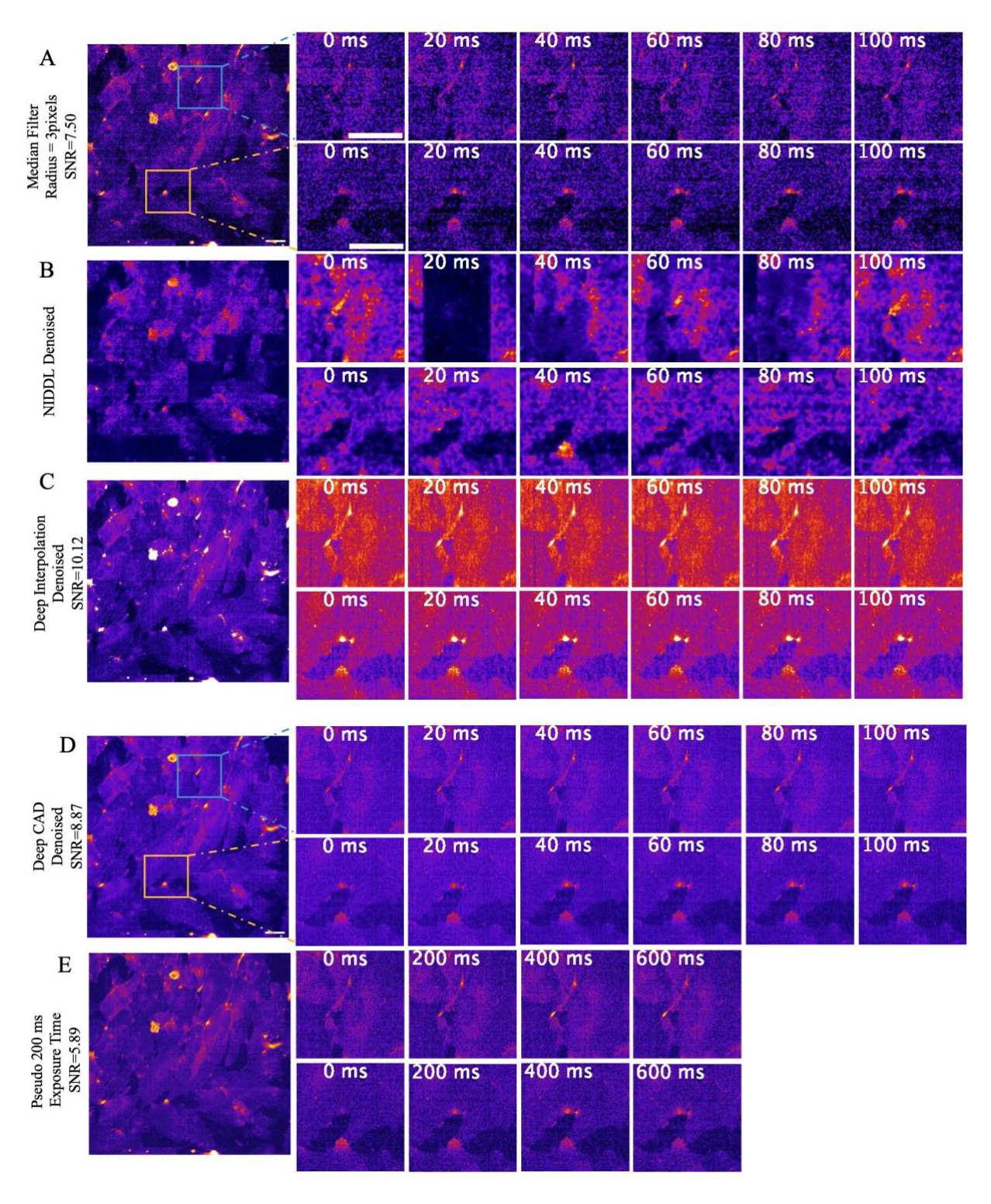


Figure 8: DeepCAD and Deep Interpolation enhances the image SNR. Denoised images following the (A) Median Filter with radius of 1pixel, (B) NIDDL algorithm, (C) Deep Interpolation algorithm, (D) DeepCAD algorithm. (E) Pseudo 200ms exposure time images from videos by adding 10 consecutive image frames using test data. The starting time in the pseudo 200ms exposure time was the same as other panels but the video had a longer duration. The right panels are zoomed in versions of the same areas at the same time points in Fig. 8. Brightness and contrast were auto adjusted for better visualization purposes. Image Size = 1024x1024. Scale bar: $40 \mu m$.

considering the excessive image artifacts generated by image processing with the algorithm. Deep Interpolation (Fig. 8C) improved the SNR \sim 2.5-fold compared to the raw data (Fig. 7B) and was \sim 40% better than the mathematical denoising (Fig. 7C, Fig. 8A).

Following processing with the DeepInterpolation algorithm the calcium signals in the denoised images appeared to be saturated, making the images look almost like binary masks (Fig. 8C). DeepCAD denoised results enhanced the SNR (Fig. 8D) by ~2-fold compared to the raw image data and the SNR was about ~20% higher than for the mathematical denoised approaches. The DeepCAD denoised result mostly closely matched the pseudo 200 ms high exposure time images (Fig. 8E).

To further explore the problem of the random blocks present in NIDDL denoised results, the three denoising algorithms were tested with 512x512 cropped and corrected images of camera noise (Fig. 9A). The NIDDL algorithm still produced these block artifacts in the denoised images (Fig. 9B). There were no artifacts generated or false positive calcium signals in the denoised images following processing with the Deep Interpolation (Fig. 9C) or the DeepCAD

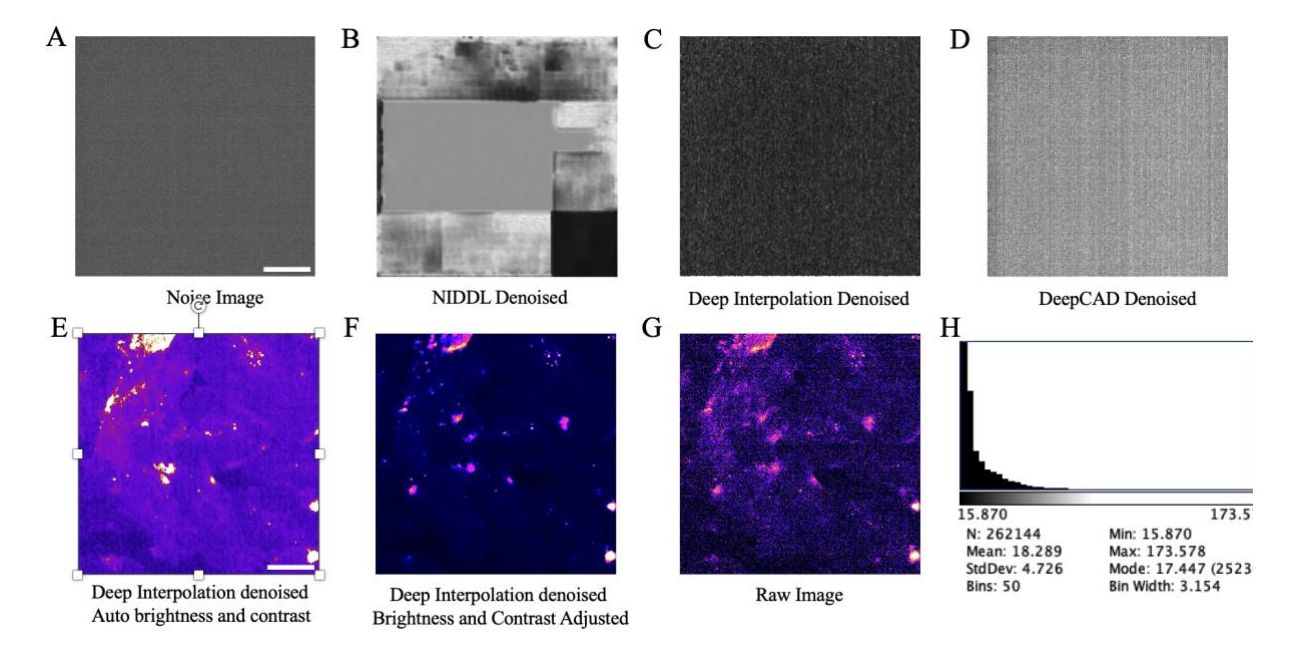


Figure 9: Deep Interpolation denoised results appear as a binary image with default image display properties and NIDDL denoised results corrupted with pure noise. (A) Camera correction image captured with no imaging slide and no illumination. Results based on the image in panel E using the (B) NIDDL algorithm, (C) Deep Interpolation algorithm, and (D) DeepCAD algorithm. (E) Denoised Deep Interpolation image displayed with auto brightness and contrast. (F) Same image in panel A but the image display settings were manually adjusted for brightness and contrast to accurately reflect the calcium flicker signals. (G) The image used to test Deep Interpolation. (H) Histogram of panel A/B. Image size: 512x512. Scale bar: $40 \mu m$.

(Fig. 9D) algorithm, confirming their reliability. Based on these results, we concluded that NIDDL did not work well with our training and test image datasets and resulted in the generation

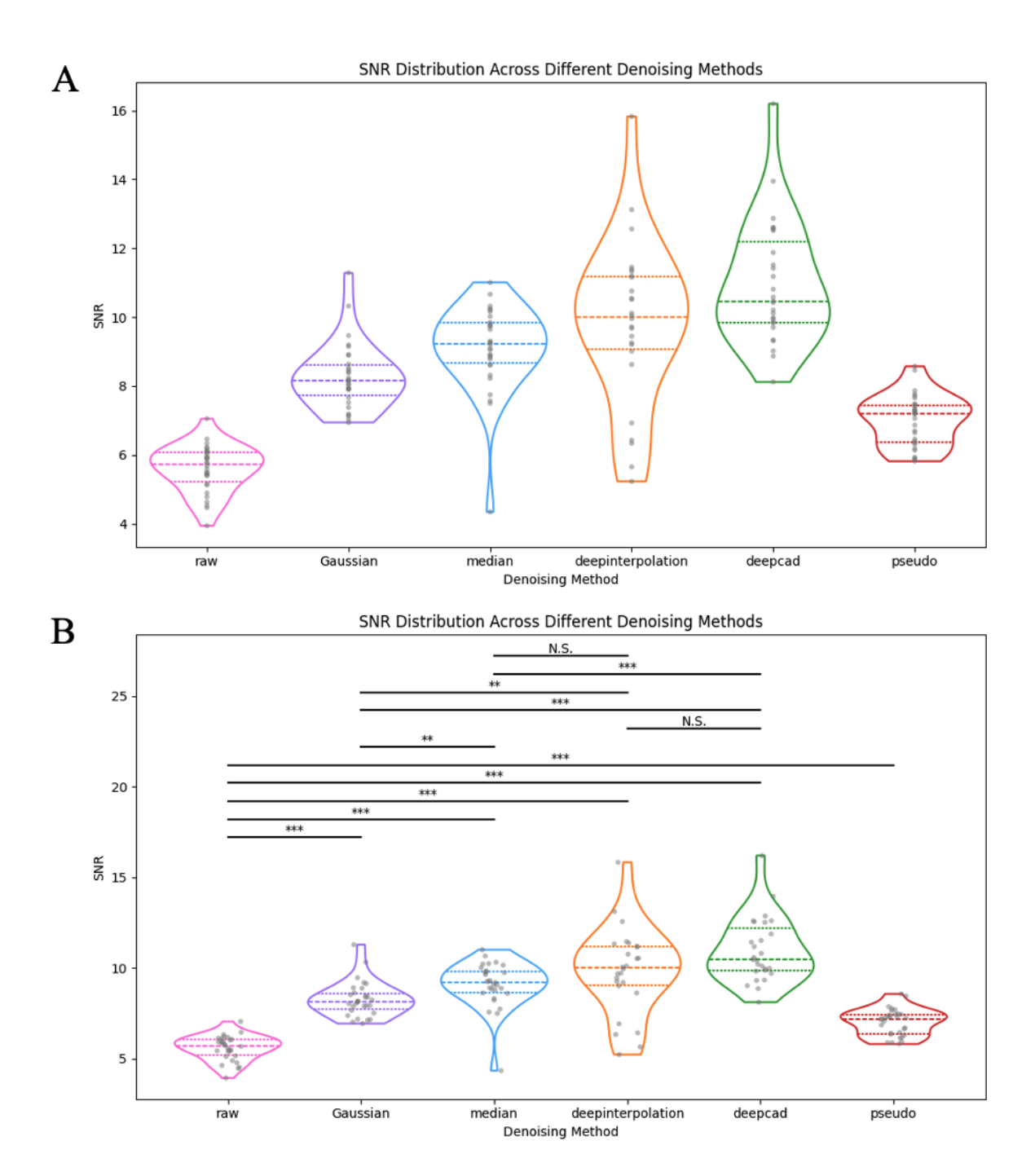


Figure 10: SNR ratio among different denoising methods. (A) and (B) were the same plot. (A) The violin plot of SNR among raw data and different denoising methods without significance for better visualization of the violin shape. (B) The same violin plot as (A) with significance. Each gray point represents SNR value of one image video stack, in (B) each data point was randomly displaced along the x-axis to prevent overlapping. The horizontal line within the violin plot represents 75% quartile, median and 25% quartile from top to bottom respectively. N=30 videos for each method and t-test. ** represents p-value < 0.01, *** represents p-value < 0.001, and N.S represent not significant.

of significant image artifacts. Due to the artifacts, NIDDL was not carried forward for the SNR analysis. Based on advice from international experts (AI4Life program -

https://ai4life.eurobioimaging.eu/) in the AI image denoising field it was decided to focus on the other two denoising algorithms that worked well. Spending significant time modifying code and adapting the NIDDL algorithm would not be a productive use of time when the other two algorithms were working well.

To examine whether DeepInterpolation denoised image results were indeed saturated or if this was only an image display issue, the images were further analyzed by adjusting the brightness and contrast and plotting an image histogram. The images only visually appeared to be saturated, and binary based on the automated image display after performing denoising. The automatic brightness and contrast were adjusted to show the background information, resulting in apparent saturation of calcium signals (Fig. 9E). If the brightness and contrast were adjusted manually to show the calcium flicker intensities accurately, the background was close to black (i.e. zero intensity) but the calcium flicker intensity signals were not saturated as no white pixels were seen in the image (Fig. 9F). Compared to the raw image intensity data (Fig. 9G), the Deep Interpolation denoised results preserved the calcium signals and lowered the background signal, leading to an improved signal-to-background ratio. The Deep Interpolate image intensity histogram demonstrates that the flicker intensity data is not saturated on the 8-bit scale (0-255) (Fig. 9H).

To further quantify the denoised image results, SNR values were calculated using 30 time-lapse image stacks acquired from 3 independent experiments. The SNR was calculated for each image stack including the raw test images, mathematical denoising (Gaussian, median), deep learning algorithms (DeepInterpolation, DeepCAD) and the pseudo 200 ms exposure time. Overall, the deep learning algorithms improved SNR significantly compared to the raw data, mathematical denoising approaches or pseudo 200 ms image data (Fig. 10). There was no significant difference between the SNR for Deep Interpolation and DeepCAD. However, Deep Interpolation showed a broader more disperse distribution of SNRs and had a few data points that had poor SNRs close to that of the raw images. The median filter achieved higher SNR compared to the Gaussian filter. Pseudo long exposure time image stacks showed enhanced SNR compared to raw data, which makes sense because it mimicked the imaging condition of 200 ms

exposure time. Based on the more in-depth SNR analysis, DeepCAD appears to provide the most robust denoising result (Fig. 10).

4.2 DeepCAD is the optimal denoising algorithm

The denoised results from Deep Interpolation and DeepCAD both looked promising, to further analyze the denoised data and determine if one algorithm was superior to the other, quantitative methods needed to be established. One direct way to compare the flickers and

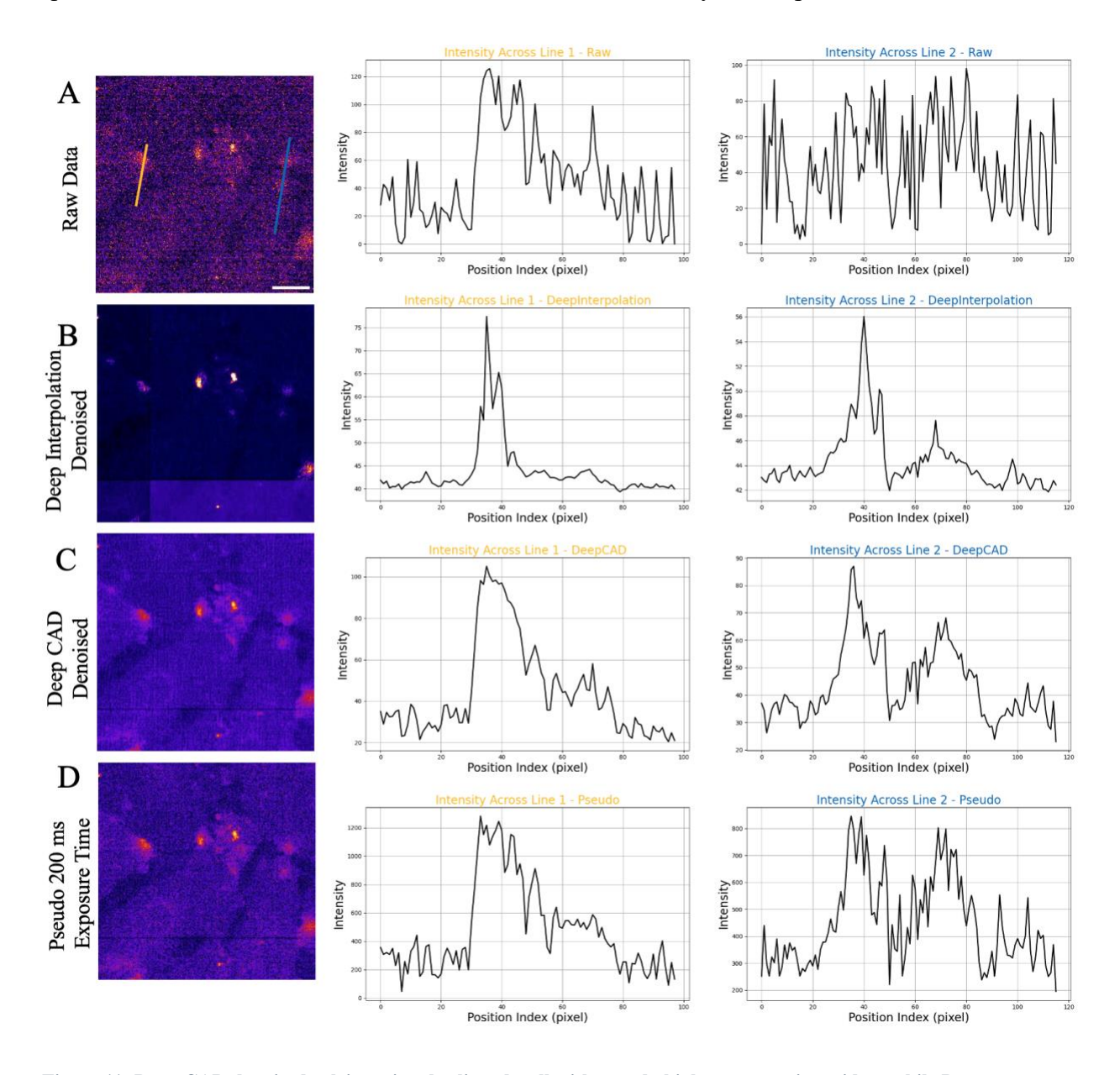


Figure 11: Deep CAD denoised calcium signals aligned well with pseudo high exposure time videos while Deep Interpolation showed slightly smaller calcium signals. (A) The intensity plot along the line 1 and line 2 in the raw image, (B) Deep Interpolation, (C) Deep CAD denoised images, (D) pseudo long exposure time (200 ms) image. Brightness and contrast were auto adjusted for better visualization purposes. Scale bar: $20\mu m$.

observe the peaks and background is by using intensity line plot profiles. Based on the intensity line plot profiles, raw data showed frequent fluctuations in the signal and the background that were often similar in magnitude (Fig. 11A). This made it difficult to characterize calcium flicker peaks (size, duration) and to distinguish calcium flicker activity from background. This also made it difficult to determine the start and end points of the flicker intensity increase and decrease representing signal initiation and signal end across the image stacks. Deep Interpolation and DeepCAD both had smoother intensity plots with higher signal and lower intensity fluctuations across the flickers and in the background (Fig. 11B, C). Following deep learning denoising algorithm image processing, it is straight forward to identify calcium flickers based on the intensity line plot profiles (Fig. 11). Deep Interpolation (Fig. 11B) had low background signals compared to DeepCAD that still showed relatively significant background intensity values (Fig. 11C). This suggests that Deep Interpolation denoised results may over correct the low intensity signals. Note that following Deep Interpolation denoising, the second peak along the shoulder on the yellow intensity plot profile is filtered out and the low intensity peak in the blue intensity plot is significantly reduced (Fig. 11B). Pseudo 200 ms exposure time intensity plot profiles showed enhanced SNRs in comparison with raw image intensity data (Compare Fig. 11A, D), with moderate fluctuations in the flicker and background intensity signals.

Since the deep learning denoising methods may change the absolute flicker intensity during denoising processes, the intensity plots were normalized to intensity values of 0-255 to enable direct comparisons among the different methods. Compared to the raw flicker intensity data, the Deep Interpolation and DeepCAD denoised data was smoother and had less fluctuations in the intensity signals (Fig. 12A, B). When compared to the pseudo 200 ms exposure time intensity data, Deep Interpolation showed lower intensity values for dimmer signals making it possible that the second calcium flicker on the blue reference line may be missed (Fig. 12C). As mentioned above, the shoulder of the calcium flicker on the yellow reference line was filtered out making the flicker appear truncated and much smaller in area (Fig. 12D). In contrast, the normalized intensity plot of DeepCAD denoised results aligned well with intensity plot data from pseudo high exposure time image intensities, confirming its accuracy of the intensity and spatial information characterizing calcium flickers (Fig. 12C, D).

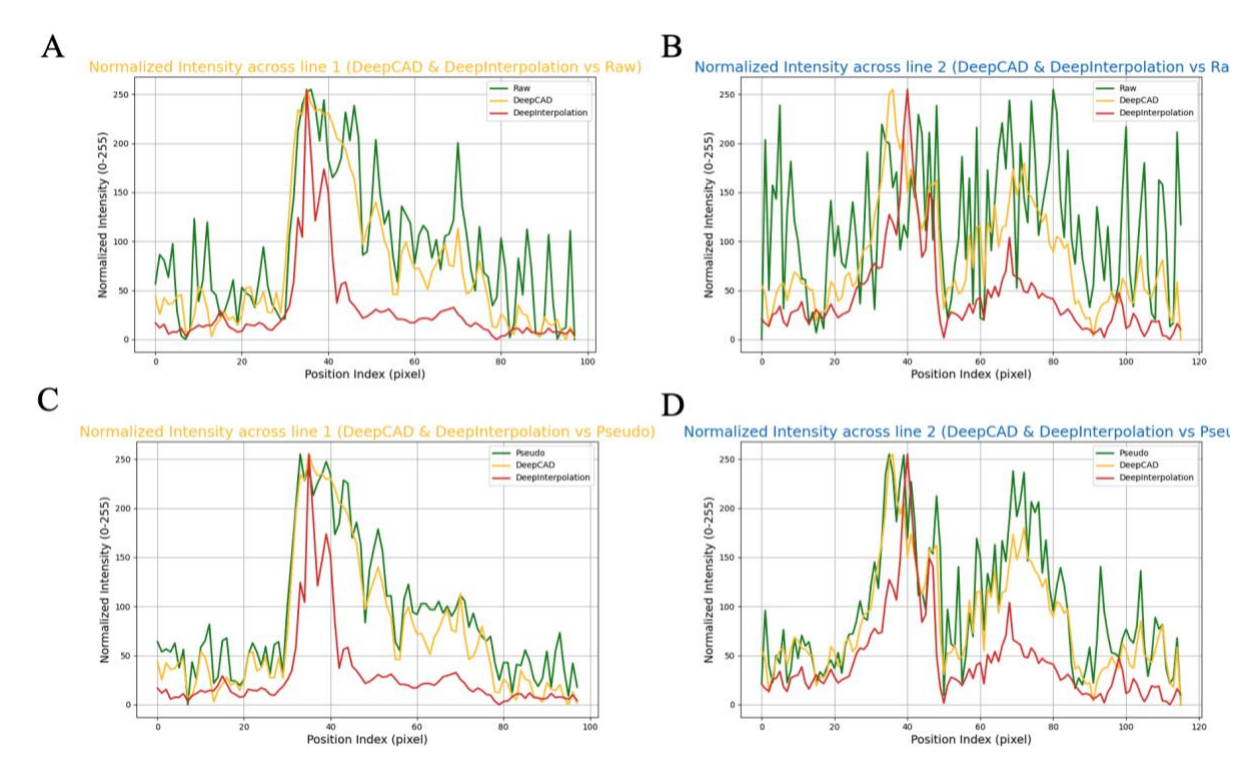


Figure 12: Normalized intensity plots among raw and multiple denoised methods. Normalized intensity plot (0-255) along (A) line1 and (B) line2 among raw data, Deep Interpolation and DeepCAD. Normalized intensity plot (0-255) along (C) line1 and (D) line2 among pseudo long exposure time, Deep Interpolation and DeepCAD. The intensity plots were based on Fig. 11.

In addition to measuring and comparing the intensity profile plots across selected calcium flickers, another quantitative method for comparison of the different denoising methods was to manually count the number of calcium flickers present in timelapse image datasets. Since the aim of this study was to determine if deep learning denoising algorithms could detect fast calcium flickers missed by current calcium imaging protocols, we hypothesized that more flickers would be detected by denoising the images captured with high temporal resolution. It is difficult to apply automated scripts to count the number of flickers present in the raw image data because of the low SNR. This made the automated process to distinguish calcium signals from the background error prone. Therefore, to ensure the consistency of the results, manual flicker counting was performed on all videos from three independent experimental replicates for all raw and denoised image data sets (Table 4).

Three experimental replicates of calcium image flicker data imaged with 20 ms exposure time were collected. The total number of calcium flickers present in each video was normalized to the number of flickers counted in the raw image data set. Deep Interpolation and DeepCAD

showed an increase in the number of flickers compared to the raw data (Table 4, Fig. 13A). DeepCAD denoising resulted in slightly more flickers compared to Deep Interpolation. Regarding the pseudo long exposure time data, it had significantly fewer calcium flickers compared to DeepCAD denoised data but a similar number of flickers compared to raw data, indicating that some low intensity flickers were missed. This is expected with long exposure time as dim intensity flickers could fade into the background with the long exposure time. Videos with 200 ms exposure times were obtained as a reference and a similar number of flickers was measured as with the pseudo 200 ms exposure time data but the 200 ms exposure data showed a much boarder distribution of numbers of flickers (Fig. 13A, B). It is not unexpected that the 200 ms image stacks had more flickers compared to the raw image data because the videos were captured at different times and the frequency of calcium flickers might be different for the same set of cells. In some cases, the 20 ms exposure time videos were captured in the same field of view but after the 200 ms exposure time videos were captured. Thus, the number of flickers in the raw 20 ms exposure time videos could have been reduced due to phototoxicity. However, control experiments on fixed cells using the same imaging conditions did not show any evidence of fluorescence photobleaching making high levels of phototoxicity unlikely (data not shown). Overall, the 200 ms exposure time video data had a very broad distribution with some videos having much fewer flickers and others many more (Fig. 13B).

Denoising methods	Raw Data	Deep Interpolation	% of Raw Data	DeepCAD	% of Raw Data
Total # of flickers	662	772	117%	865	131%
# of flickers with a duration <200 ms	103	64	62%	108	105%

Table 4: Number of total and fast flickers in different videos. Total number of flickers was counted manually and the number of flickers with a duration less than 200ms was counted using automated scripts.

To further explore the characteristics of the detected flickers in the raw versus denoised timelapse videos, an automated detection script was developed and used to extract the duration, intensity and area information of each detected flicker. In this case, the total number of flickers was lower than the number counted manually but this enabled automated segmentation and measurement of flicker properties. Automatically detected flickers with a duration <200 ms accounted for 15.6%, 8.3% and 12.5% of the total number of flickers for the raw, Deep Interpolation or DeepCAD denoised data respectively (Table 4). When looking only at the fast

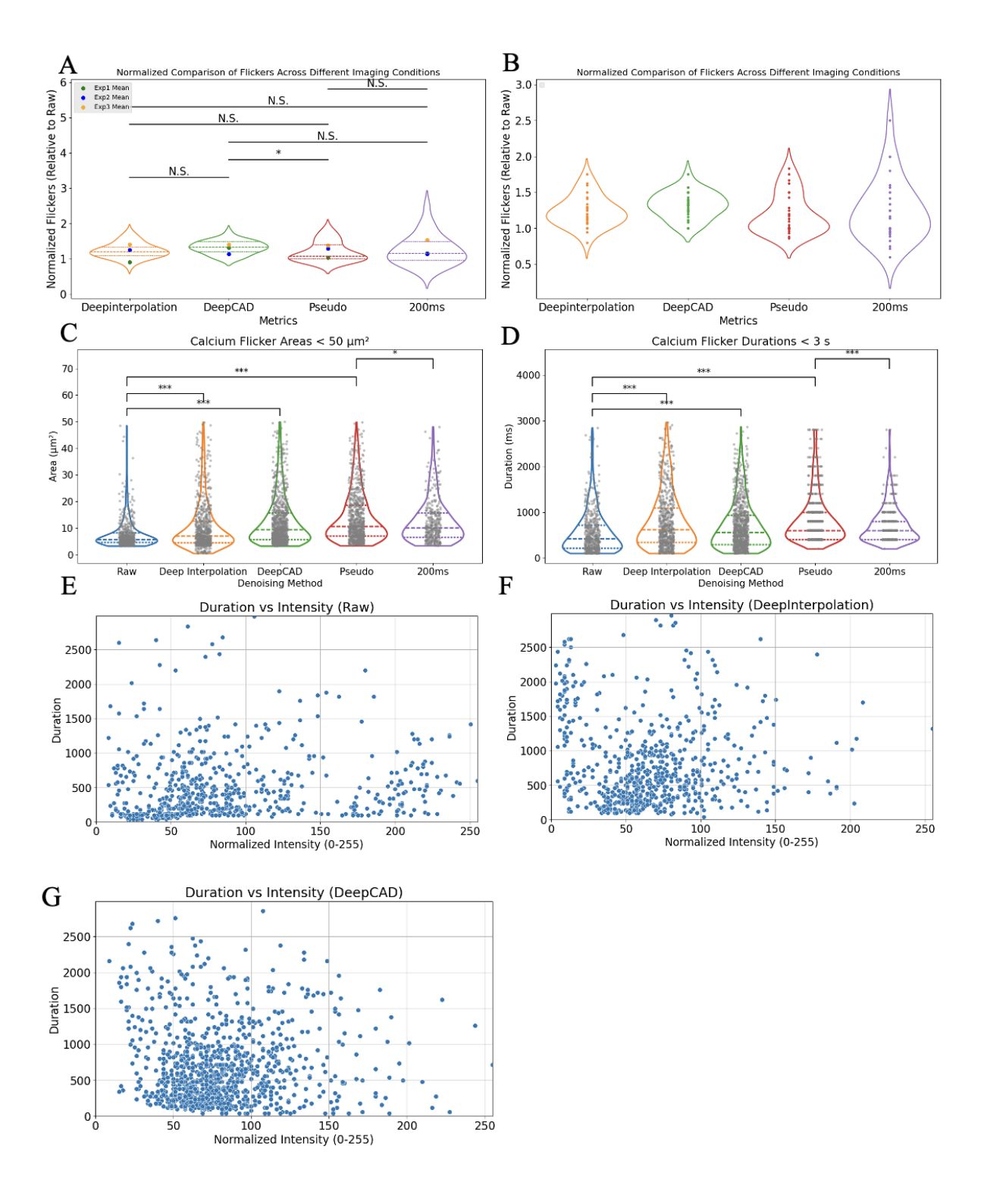


Figure 13: Denoising methods detect more dim calcium flickers with longer durations. (A) Violin plot of the number of flickers present in each image video stacks normalized to raw data. Each dot inside the violin plot represents the mean of each experiment. N=30 for each method. (B) Same plot as panel (A) but includes individual data points for each video. (C) Violin plot of the area of calcium flickers detected by the automated detection script. The plot was filtered to show flickers with an area smaller than $50 \, \mu \text{m}^2$ for better visualization. (D) Violin plot of the duration of calcium flickers detected by the automated detection script. The plot was filtered to show flickers with a duration shorter than 3000 ms for better visualization. The horizontal line within the violin plot represents 75% quartile, median and 25% quartile from top to bottom respectively. N.S. represents not significant, * represents p-value < 0.05, ** represents p-value < 0.01 and *** represents p-value < 0.001. Individual data points were randomly displaced along the x-axis to prevent overlapping. Scatter plot of duration and intensity of calcium flickers detected by the automated detection script in (E) raw data (F) Deep Interpolation, (G) DeepCAD. Each blue point represents a single flicker. The intensity was normalized to 0-255.

flickers, Deep Interpolation missed ~38% of them while DeepCAD detected essentially the same number as in the raw data. The loss of flickers following Deep Interpolation denoising is likely due to the over correction of the background and loss of low intensity flickers. Interesting, this indicated that most fast flickers can be captured without denoising so they must be bright enough to be distinguished from the noisy background and the extra flickers detected by DeepCAD might be low intensity flickers with slower dynamics.

The area of the automatically detected calcium flickers from the 30 videos was measured for the raw and denoised image data sets. Deep Interpolation were the only images that had a large populations of calcium flickers with a smaller size (Fig. 13C). This further confirms the previous finding that Deep Interpolation denoising results in dim flickers disappearing and large flickers appearing much smaller than they really are (Figs. 11, 12). This is expected as the Deep Interpolation algorithm resulted in a dark image background indicating low intensity data clipping. DeepCAD had a similar distribution of flicker area as pseudo and actual 200 ms exposure time videos and all three captured more flickers with a size larger than 20 µm² (Fig. 13C). Deep Interpolation and DeepCAD denoising also resulted in the detection of more flickers with a duration greater than 2000 ms (Fig. 13D). This aligns with the previous conclusion that the low SNR in raw image data can cause inaccurate identification of the starting and ending timepoints of the flicker signal, leading to a truncated or shorter calcium flicker duration.

Scatter plots were made using raw, Deep Interpolation and DeepCAD denoised data to further explore the distribution of the flicker data and any relationship between different flicker characteristics. A Duration versus Normalized Intensity plot of the Raw flicker data shows a scatter plot with flicker durations up to ~3000 ms (3 s) and normalized intensities from 0-255 (Fig. 13E). The majority of flickers had a duration of less <1000 ms. Interestingly, the longest duration flickers also correspond to lower intensity flickers. Deep Interpolation shows a shift to

lower normalized intensities with a large number below 20 intensity units demonstrating that the denoising algorithm clips the low intensity data from the images (Fig. 13F). DeepCAD showed

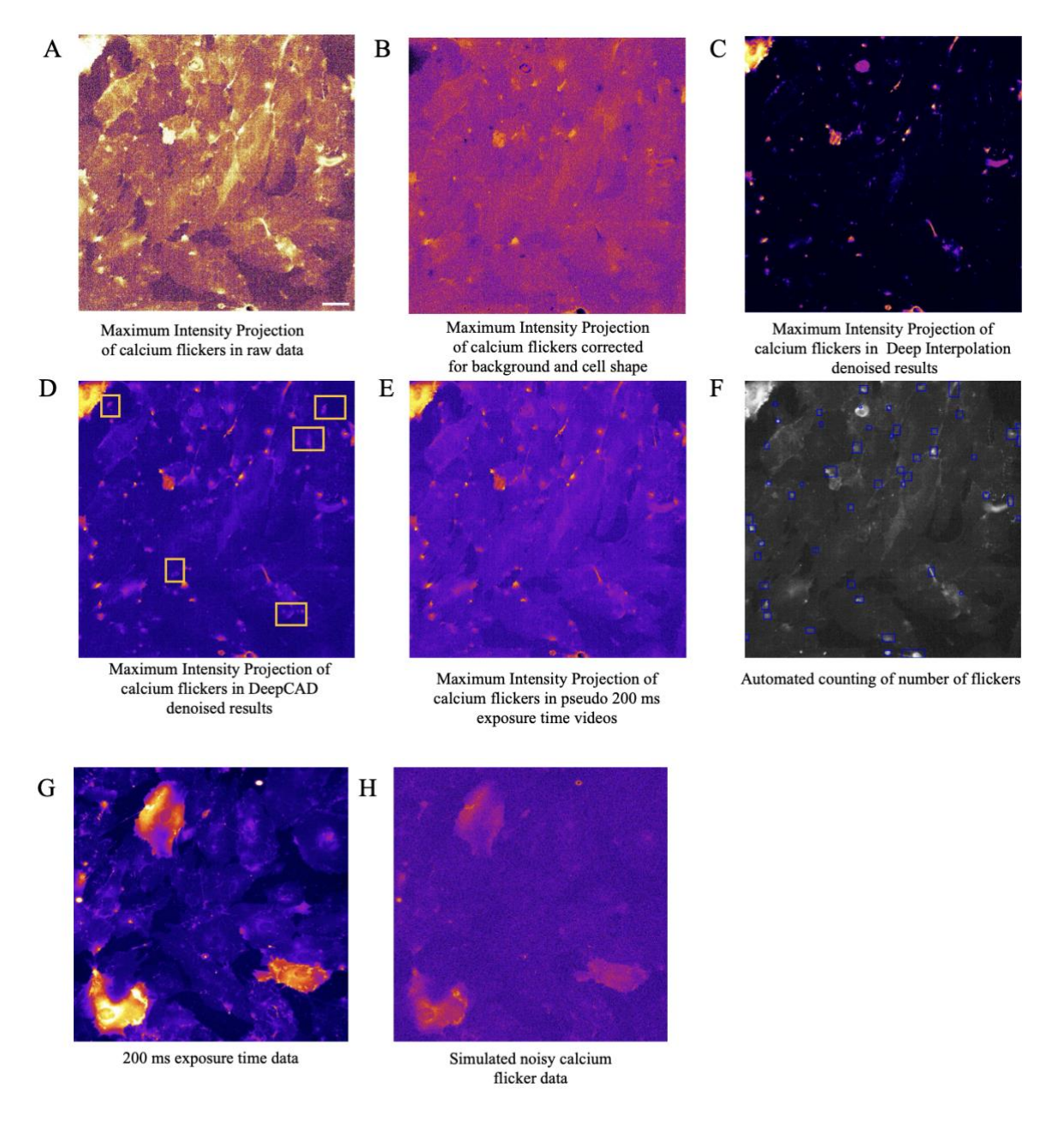


Figure 14: Denoising algorithms detect more calcium flickers compared to raw data. Maximum intensity projection (MIP) of (A) raw data, (B) raw data corrected for background and cell shape, (C) Deep Interpolation, (D) DeepCAD denoised results and (E) pseudo long exposure time videos. (B) was the MIP for the first 20 frames for better visualization and all other MIPs were for the entire test image stacks. Yellow boxes in (C) highlight some examples of low intensity flickers that were detected by DeepCAD and not detected in raw and pseudo 200 ms exposure time videos. (F) Mask of automated counting the number of flickers present in time lapse images. Each blue box represents a detected calcium signal in DeepCAD denoised data. (G) 200 ms exposure time high SNR data, served as ground truth data for simulated noisy calcium flicker data. (H) Simulated noisy calcium flicker data by adding Poisson and Gaussian noise to 200 ms exposure time data. Brightness and contrast were auto adjusted for better visualization purposes. Image Size = 1024×1024 . Scale bar: $40 \mu m$.

more flickers in the upper left corner of the plot which represents the long duration and low intensity flickers (Fig. 13G). There was a portion of bright flickers lost in the DeepCAD data that could be the result of an artifact caused by the change of intensity during the denoising process (Fig. 13G). Overall, DeepCAD denoising improves the detection of low intensity long duration flickers likely due to the ability to detect the flickers early and late in their dynamic process when they are dim. These long duration flickers of variable intensity are not detected in the raw data and the low intensity ones are filtered out with the DeepInterpolation denoising algorithm.

Maximum intensity plots were used to visualize all the flicker activities present throughout the entire timelapse videos. Looking back at the data, the small dim flickers were easily missed in the raw data because the background was noisy, and it was difficult to distinguish whether it is a true signal or random noise (Fig. 14A-E). Automated counting of calcium flickers was developed to facilitate the counting process and visualized the detected flickers by drawing a blue box around each detected flicker (Fig. 14F).

Simulated low SNR 200 ms calcium data was generated by adding Poisson and Gaussian noise to 200 ms exposure time videos to further validate the denoised results (Fig. 14G, H). For each detected flicker in the original 200 ms exposure image data. Time overlaps for individual flickers according to the start and end frame were checked by comparing the same flicker in the original 200 ms exposure time image with the denoised results of simulated low SNR images. Deep Interpolation achieved 61% precision in detecting flickers and recovered 26% of the flickers while DeepCAD had a precision value of 60% and retrieved 78% of the flickers (Table 5).

Methods	Deep Interpolation	DeepCAD	
# of flickers in 200 ms exposure time videos in 5 seconds	211		
# of flickers in denoised videos	88	276	
# of matched flickers	54	164	
Precision Value	0.61	0.60	
Recall Value	0.26	0.78	

Table 5: Accuracy and recall value of Deep Interpolation and DeepCAD denoised results. The precision and recall value were calculated using 3 independent videos.

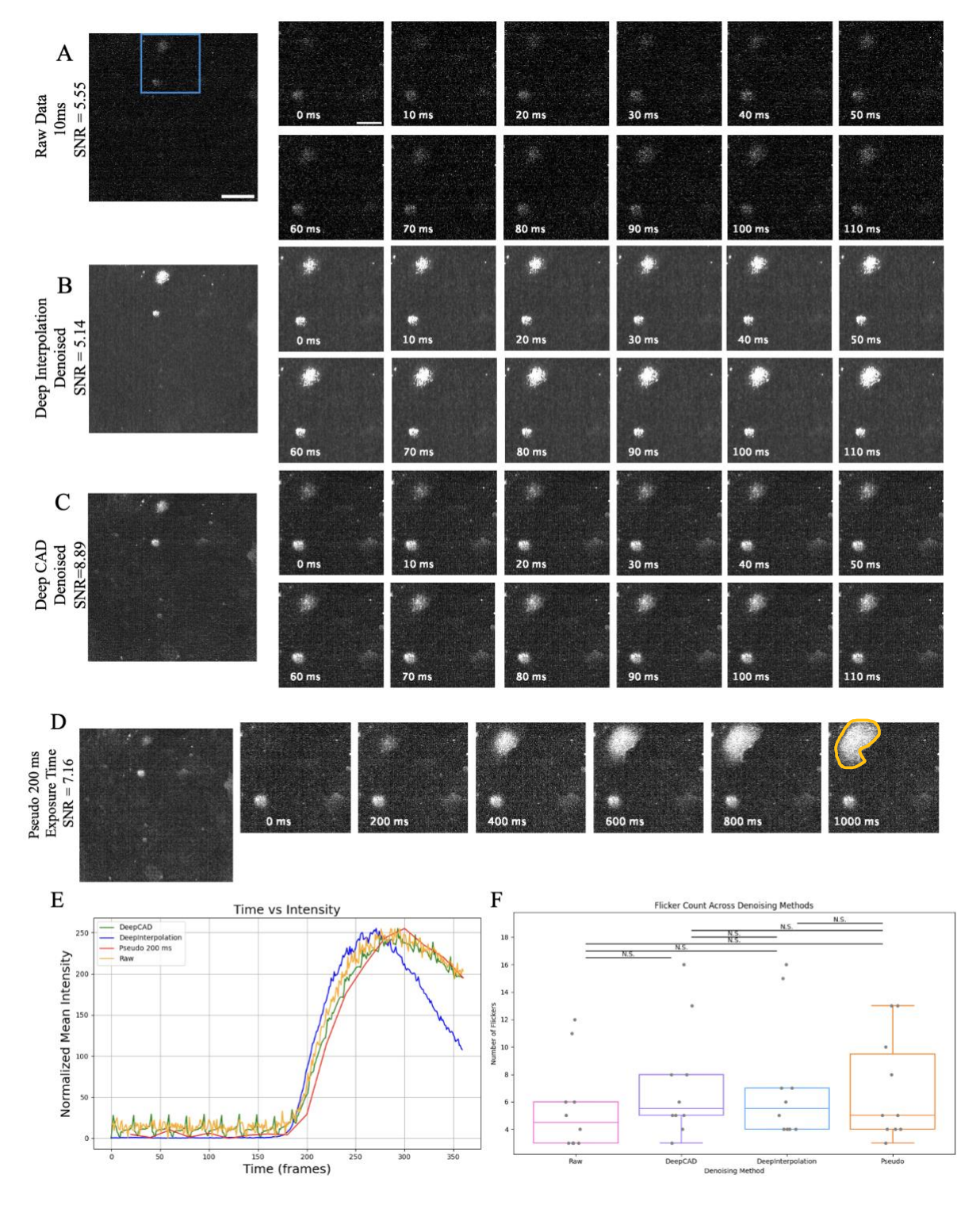


Figure 15: DeepCAD denoises images captured at a short exposure time of 10ms. (A) Test raw data imaged at 10 ms, 100 fps. Denoised image using (B) Deep Interpolation, (C) DeepCAD denoising models and (D) Pseudo 200 ms exposure time videos by adding together 20 consecutive image frames using the test data. The second frame in the pseudo 200 ms exposure time was at the same time point as other panels but has a longer duration. The right panels are zoomed in images of the blue box region. Image Size = 512x512. Scale bar: 40 μm. Normalized mean intensity of the area of interest, the calcium wave originated from localized calcium activity, illustrated by the yellow annotations in panel (D), in (E) raw data, DeepInterpolation, DeepCAD denoised results and pseudo 200 ms exposure time videos. (F) Box plot of number of flickers present in each video using different denoising methods. N=10 videos. The upper and lower bounds of the box indicate 75% and 25% percentiles respectively and the middle line inside the box indicated 50%. The whiskers represent the maximum and minimum values of each box plot. Each gray dot represents the number of flickers in one video. Data points outside the box were outliners. N.S. represents not significant.

4.3 DeepCAD can push the temporal limit of calcium imaging to 10 ms or 100 fps

To further test the temporal limit of the denoising algorithms, timelapse images with an even shorter exposure time of 5 or 10 ms were obtained as additional test datasets for Deep Interpolation or DeepCAD denoising. Since there were few calcium flickers present in the raw data, it was not possible to quantify the SNR in the raw data with 5 and 10 ms exposure time image videos. Comparing to images captured at 20 ms exposure time (Fig. 7B), images at 10 ms exposure time were much nosier and it was difficult to visualize the flicker intensity signals relative to the background (Fig. 15A). Deep Interpolation denoised images had a slightly lower SNR compared to raw data (Fig. 15B) while DeepCAD was able to denoise images and improve SNR by ~2-fold (Fig. 15C). The flicker on the top left of the 10 ms denoised images (Fig. 15B, C) clearly showed the propagation of the calcium flicker in space and time. In comparison, the pseudo 200 ms exposure time images (Fig. 15D) that do not resolve the flicker dynamics with high precision. Based on the plots of normalized mean intensity over time, raw data showed the propagation and diffusion of calcium waves with moderate fluctuations while DeepInterpolation and DeepCAD denoised results had minor fluctuations (Fig. 15E). Deep Interpolation denoised results showed clipped calcium activity as the flicker intensity started to decrease earlier after the peak compared to other methods (Fig. 15E). For bright flickers, pseudo 200 ms exposure time videos had a similar temporal flicker shape of the plot compared to raw image data and DeepCAD denoised results, but the points were dispersed, leading less well-defined flicker intensities over time (Fig. 15E). The total number of flickers present in raw and denoised videos were manually counted and there was an increase in denoised videos compared to raw data but the difference was not significant (Fig. 15F). There was no significant change in the total number of flickers in raw and pseudo long exposure time videos. Perhaps with additional data collection there could be a significant difference in flicker detection with denoising.

Calcium flickers were not visible in raw images captured with a 5 ms exposure time (Fig. 16A) and were barely visible with Deep Interpolation (Fig. 16B) or DeepCAD (Fig. 16C) denoising. Even with the pseudo long exposure time images, both the calcium flicker and the background were hard to distinguish due to the noise contribution from adding together 40 short exposure images (Fig. 16D) when compared to a single image captured with a 200 ms exposure time (Fig. 16E). It would be difficult to study the localization of the flickers with 5 ms exposure

time data because the cell shape is not visible. Deep Interpolation and DeepCAD restored the calcium signals from the raw data but they are still difficult to detect.

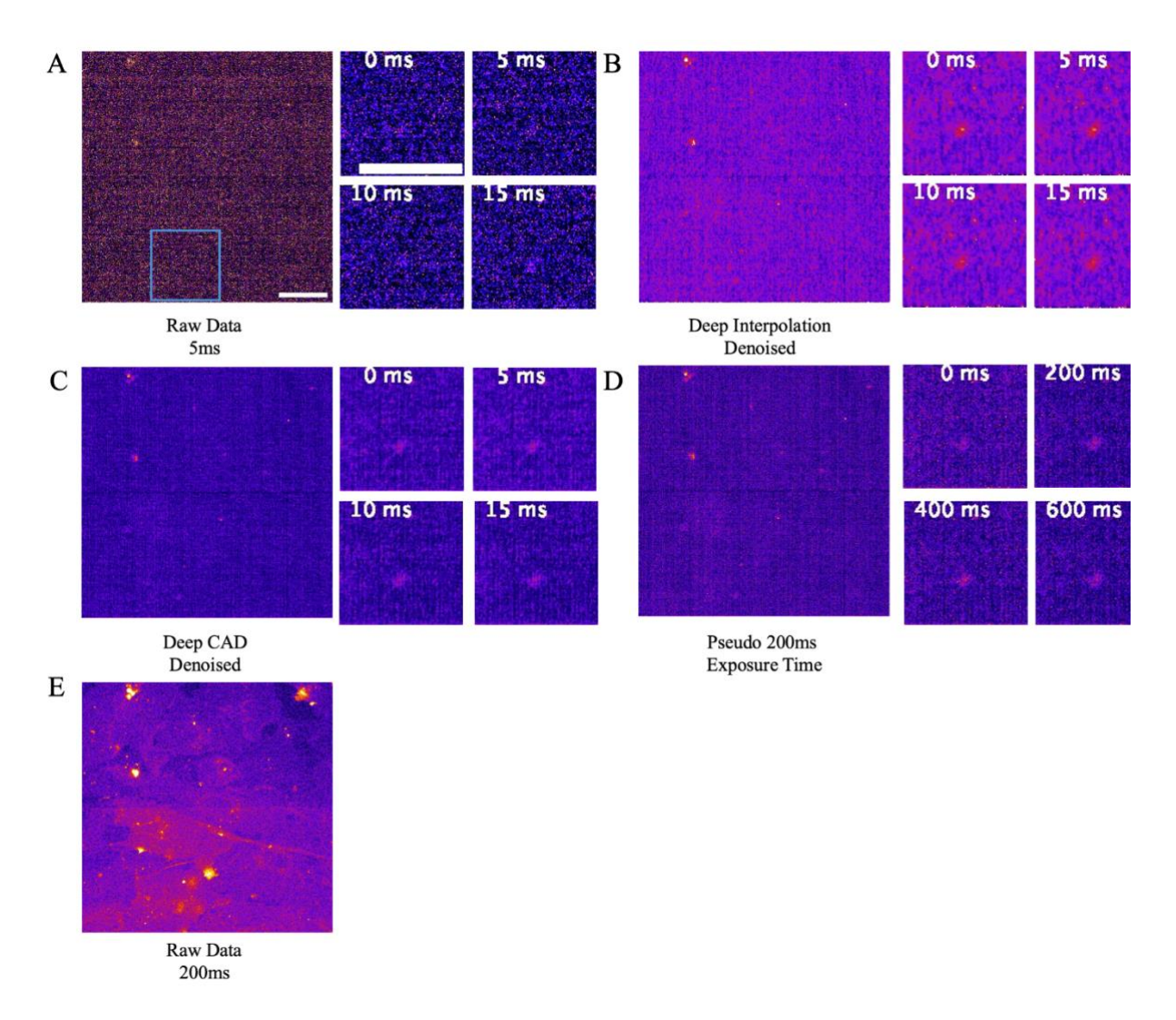


Figure 16: Deep Interpolation and Deep CAD recover the signal from noisy images captured with a 5 ms exposure time but cell shape and background information is not revealed. (A) Test raw data imaged at 5 ms, 200 fps, center camera quadrant. (B) Denoised image using Deep Interpolation, (C) Denoised image using DeepCAD and (D) Pseudo 200ms exposure time image created by adding together 40 consecutive image frames using the test data. The starting time point in the pseudo 200 ms exposure time was the same as other panels but has a longer duration. The right panels are zoom in images of the data within the blue box. Brightness and contrast were auto adjusted differently for each image panel for better visualization purposes. Image Size =512x512. Scale bar: $40 \mu m$.

5 Discussion

This project aimed to develop a fast calcium imaging protocol with optimal spatial and temporal resolution using deep learning denoising algorithms. There are many denoising algorithms mentioned in the introduction section, but most of them are not based on calcium imaging. Three calcium denoising algorithms of different types including supervised and unsupervised algorithms were chosen and compared to determine the performance of these different deep learning models (Table 3). Based on several factors it was determined that DeepCAD was the best algorithm for denoising the calcium imaging data collected during this project.

DeepCAD was easiest to install and had clear instructions. Many problems were encountered with NIDDL and Deep Interpolation in terms of setting up the environment. For NIDDL, the instructions were confusing and difficult to follow, and some scripts are hard coded for reading and processing the image files, so the users need to either follow the name restrictions in the code or directly modify the scripts. This makes this algorithm difficult for non-experts to install and use. NIDDL did have a clear and complete explanation for TensorFlow, but it is built on an out-dated TensorFlow version that cannot be installed on the DRAC advanced computing resource. Only limited instructions were available for the PyTorch version of the algorithm but that did work. Deep Interpolation requires a large amount of training data and powerful advanced computing units. Based on the training experience for this work, even when it was trained with a powerful GPU (Tesla 4) it was slow. It took about 4 hours for Deep Interpolation to train on a single video while DeepCAD took less than 1 hour for the same video. This is a major limiting factor for implementing Deep Interpolation and especially for research groups that do not have access to advanced computing resources and expert computer scientists.

Most deep learning denoising models are designed for mouse brain images captured with a multi-photon microscope^{53,59,60}. In neuroscience, live cell imaging sometimes needs multiphoton infrared imaging to go deep into the tissue and some neurons are sensitive to visible light^{53,59,60}. Scattering in tissue and the need to minimize excitation light can lead to insufficient illumination conditions and low signal to noise images. For all live cell imaging experiments there is a desire to reduce the illumination light power and/or exposure time to minimize photobleaching and phototoxicity and maintain sample health⁶⁹. By applying denoising methods, the illumination light power and/or duration can be decreased to reduce phototoxicity and keep cells healthy throughout the imaging session. These methods can also improve the SNR for images collected deep within tissue. As discussed in this thesis, denoising can make rapid imaging possible by reducing the necessary camera exposure time while maintaining a satisfactory SNR to identify objects or events of interest. Previous studies obtained their low SNR images by using low laser power on a confocal microscope^{53,59,60}. Here the images had low SNRs because the exposure time was short. The goal of this work was to apply denoising methods to improve the SNR allowing high speed imaging of calcium signals with cultured cell monolayers.

All the denoising methods including mathematical filters and deep learning denoising algorithms enhanced SNR significantly but deep learning models outperformed traditional mathematical methods. Among the selected deep learning algorithms, NIDDL did not work for our training and testing datasets because it introduced many artifacts in denoised images that interfered with imaging of calcium flickers. So, we focused on comparing Deep Interpolation and DeepCAD denoising to improve calcium flicker detection and characterization. Both of them detected more flickers compared to raw data, but Deep Interpolation reduced the flicker size,

clipped low intensity flickers and only detected ~62% of fast flickers. DeepCAD retrieved dim flickers without altering the biological structures.

Traditional mathematical filters like Gaussian and median filters improve the SNR of the image but they caused image blur at the same time. This can impact the flicker characteristics by possibly changing the flicker area and under or overestimating it relative to raw data. Although the mathematical filters are relatively easy to use, the processing time is nearly instantaneous and ImageJ/Fiji has the built-in function of different mathematical filters, they didn't improve SNR as much as deep learning algorithms (Fig. 10) so they were not pursued further.

Unfortunately, NIDDL resulted in many image artifacts after training and testing with our image datasets. One possible reason for this is the difference in the training dataset relative to the original study. The original low and high SNR dataset⁵³ used by *Chaudhary et al.* was obtained with calcium signals in live mouse brains and the time differences between the two stacks was short (~100 ms) compared to the dynamics of calcium signal in neurons. So, the paired images used for training contained similar temporal information. In our case, we used fixed cells to generate paired images with the same signals for training the algorithm. This is because there would have been significant changes in the calcium flicker signals in the HUVEC monolayers with a 100 ms time difference between images. However, the original live cell data used to train NIDDL could have had temporal features in the image data that were critical for algorithm training. So some of the image artifacts could be a result of training on static calcium flicker image data with only the noise varying. After careful discussion with international AI image analysis experts from the Euro Bio-Imaging AI4Life program, it was decided to move on with the two other denoising algorithms that were working well and not to try to resolve, recode or retrain NIDDL.

Based on the Deep Interpolation results, it is tempting to recognize the denoised results as a binary image. After checking the histogram, it determined that this was only an image display problem, resulting from the fact that the Deep Interpolation algorithm reduces background so much that many pixels are black and read zero intensity units (Fig. 9E, F). This benefits segmentation tasks and increases the image SNR since there is minimum background signals. Deep Interpolation enhanced the image SNR significantly compared to raw data (Fig. 10), but by looking at the intensity plot of flickers following Deep Interpolation denoising, it was clear that the algorithm clips low intensity data from the images, minimizes the size and peak intensity of the flickers and changes their spatial (Fig. 11, 12 and 15E) and temporal shape. This then alters the biological features that are being measured and resulted in many low intensity flicker signals being removed from the images and the analysis as they were below the detection range for both manual and automated flicker detection and counting (Table 4). Based on the results of simulated low SNR calcium flicker data, Deep Interpolation only detects about 26% flickers compared to 200 ms exposure time image data (Table 5).

DeepCAD was the best denoising approach for the datasets under study during this thesis work for many reasons. The flicker sizes were similar to those in the pseudo long exposure time or 200 ms exposure time image data sets (Fig. 14B). It gives the best SNR without any apparent image artifacts (Fig. 16C, D) and DeepCAD denoised images resulted in the detection of the highest number of calcium flickers from the test dataset (Table 4, Fig 13). The original hypothesis for this thesis was that with faster imaging rates and deep learning-based image denoising more fast calcium flickers would be detected. It turned out that the fast flickers were bright enough to be identified in raw image data with 20 ms exposure times (Table 4). However, DeepCAD denoising resulted in the detection of additional flickers that corresponded to dim

flickers with a long duration (Fig. 14B-F). In principle, with fast imaging at 100 fps the DeepCAD denoising models can capture fast flickers that could otherwise be missed by current imaging protocols and low intensity flickers occurring on any timescale that would normally be lost in the noisy background of short exposure images. In addition, the flicker duration is more accurate because when the flickers are dim at the start and end of the flicker event are determined more accurately. DeepCAD seems to generate a small intensity periodic intensity peak across the data. This phenomenon needs further investigation to determine how this artifact arises and find ways to mitigate it (Fig. 15E). Although in some cases Deep Interpolation shows higher SNR this is due to the fact that it is clipping low intensity data resulting in loss of features within the images. In addition, DeepCAD retrieved 78% of flickers while Deep Interpolation only recovered 26% when tested with simulated low SNR calcium image data (Table 5). The fact that that 22% of flickers remain undetected demonstrates that more work needs to be done to improve DeepCAD denoising. Thus, DeepCAD is preferred as it detected dim flickers that are missed in the raw 200 ms exposure time data, it does not clip low intensity data like Deep Interpolation but further improvements are needed.

The automated calcium flicker detection script detects ~80% calcium flickers for raw image data and achieving an accuracy of ~90% for denoised data. This reduced manual labor efforts and allowed for the detailed measurement of flicker numbers, area and duration. It is always tricky to quantify the effectiveness of an unsupervised model because it does not have ground truth data to compare to. In live cell imaging, each cellular event is random and unique so it is impossible to capture the exact same event twice with different imaging conditions. In this study, we generated pseudo-long exposure time videos so that the performance of different denoising methods could be evaluated.

For deep learning denoising methods, the denoised images are generated from the input data. It is possible that the deep learning model generates something that does not exist or is not reflected in the raw data (like what was observed with the NIDDL algorithm), also known as a false positive. Vice versa, there can also be false negatives which refer to the situation when the model removes signals that are present in the raw data. To ensure that the denoised results were accurate with no extra synthetic signals and no signals missing, simulated calcium data is the optimal method to choose. By using simulated calcium data, the exact number, intensity, area, duration and location of calcium flickers would be known. The denoised results could then be examined to determine its accuracy and if any false flickers are generated or real flicker signals are removed in the denoised images. Current simulated calcium data are mostly based on calcium signals in neurons⁷⁰, and there is no existing synthetic calcium flicker data for cultured cell monolayers. Future work can be done to generate simulated calcium flicker data similar to what is seen in the HUVEC cell models and it could be used to evaluate the performance of denoising algorithms.

The main goal is that DeepCAD detects low intensity flickers that are missed otherwise. It more accurately captures the temporal flicker characteristics including accurate identification of flicker initiation and flicker duration. With the 20 ms resolution we can more accurately characterize the flicker area and temporal signal and duration, while minimizing phototoxicity and photobleaching in live samples by reducing light exposure. Based on the current denoising results, using the imaging set up and conditions developed during this project, the temporal resolution of calcium flicker imaging can be optimized for rapid 100 fps live cell imaging. This is 20x faster than the current optimized protocol being used for the system. One possible reason that the denoising models didn't work well for images captured with 5 ms exposure time was that

the input image was so noisy that there are no obvious calcium signals that the model can refer to and predict on (Fig. 17A). It is possible that retraining DeepCAD with 5 ms exposure time training data from fixed and/or live samples could improve its performance. Other possibilities to improve temporal resolution could include: 1) increased excitation light power to improve the image SNR with short exposure times improving the image quality to determine if the denoising model can generate high SNR denoised images, 2) use of a more efficient microscope light emission light path, or 3) use of a more sensitive camera detector. Interestingly, it was not rapid flickers but low intensity flickers that DeepCAD was able to pull out of the noise of raw images. In the future, the ability to image rapidly could be used to multiplex and add 1) a second or third fluorescence channel, 2) rapid tiling of large sample areas or 3) z-stacks for 3D imaging.

From the perspective of the biological sample and the calcium sensor, these experiments were conducted with the GCAMP-6s calcium indicator. Recently, a faster and more sensitive family of GCAMP-8[f,m,s] calcium indicators were developed⁷¹, with enhanced brightness and faster rise and decay times with t_{1/2} of 10 ms and 100 ms, respectively. This will improve the spatial and temporal resolution because of improved brightness and help with the detection of fast and low intensity flickers while minimizing phototoxicity to ensure sample health. These new sensors will also reflect the calcium dynamics more accurately and help improve measurements of the dynamics and characteristics of calcium flickers. Further studies can be done using the fast calcium imaging protocol developed here to investigate the origin of calcium waves and better identify the characteristics (e.g. size, rise time, decay time, frequency, duration) of calcium flickers, which should help understand the fundamental biological functions of calcium flickers.

6 Conclusion

In summary, we have accomplished our goal of developing an optimized calcium imaging protocol with enhance temporal resolution using deep learning denoising methods. Among the selected denoising algorithms, DeepCAD outperformed the other two in enhancing SNR. It also retrieved the highest number of dim flickers from the raw videos and the structure of detected flickers were accurate and similar to pseudo high exposure time images. Using denoising algorithms, fast calcium imaging can be achieved and fast and/or dim calcium flickers that are missed by current calcium imaging protocol can be identified and characterized. With DeepCAD, the temporal resolution limit can be pushed up to at least 100 fps. The new protocol enables rapid calcium imaging while maintaining optimal spatial resolution and SNR with no evidence of phototoxicity. In the future, it can be used as a power tool to perform fast calcium imaging to study transient cellular events. It could also be applied to study other rapid cellular events or characterize low intensity features within biological samples.

References

- 1. Vannucci L, Fossi C, Quattrini S, et al. Calcium Intake in Bone Health: A Focus on Calcium-Rich Mineral Waters. *Nutrients*. Dec 5 2018;10(12)doi:10.3390/nu10121930
- 2. Sudhof TC. Calcium control of neurotransmitter release. *Cold Spring Harb Perspect Biol.* Jan 1 2012;4(1):a011353. doi:10.1101/cshperspect.a011353
- 3. Kuo IY, Ehrlich BE. Signaling in muscle contraction. *Cold Spring Harb Perspect Biol*. Feb 2 2015;7(2):a006023. doi:10.1101/cshperspect.a006023
- 4. Tsai F-C, Kuo G-H, Chang S-W, Tsai P-J. Ca²⁺ Signaling in Cytoskeletal Reorganization, Cell Migration, and Cancer Metastasis. *BioMed Research International*. 2015/04/22 2015;2015:409245. doi:10.1155/2015/409245
- 5. Prevarskaya N, Ouadid-Ahidouch H, Skryma R, Shuba Y. Remodelling of Ca2+ transport in cancer: how it contributes to cancer hallmarks? *Philos Trans R Soc Lond B Biol Sci.* Mar 19 2014;369(1638):20130097. doi:10.1098/rstb.2013.0097
- 6. Chen YF, Chen YT, Chiu WT, Shen MR. Remodeling of calcium signaling in tumor progression. *J Biomed Sci*. Apr 17 2013;20(1):23. doi:10.1186/1423-0127-20-23
- 7. Vorotnikov AV. Chemotaxis: movement, direction, control. *Biochemistry (Mosc)*. Dec 2011;76(13):1528-55. doi:10.1134/S0006297911130104
- 8. Li S, Huang NF, Hsu S. Mechanotransduction in endothelial cell migration. *J Cell Biochem*. Dec 15 2005;96(6):1110-26. doi:10.1002/jcb.20614
- 9. SenGupta S, Parent CA, Bear JE. The principles of directed cell migration. *Nat Rev Mol Cell Biol*. Aug 2021;22(8):529-547. doi:10.1038/s41580-021-00366-6
- 10. Lammermann T, Sixt M. Mechanical modes of 'amoeboid' cell migration. *Curr Opin Cell Biol*. Oct 2009;21(5):636-44. doi:10.1016/j.ceb.2009.05.003
- 11. Huttenlocher A, Horwitz AR. Integrins in cell migration. *Cold Spring Harb Perspect Biol.* Sep 1 2011;3(9):a005074. doi:10.1101/cshperspect.a005074
- 12. Lintz M, Munoz A, Reinhart-King CA. The Mechanics of Single Cell and Collective Migration of Tumor Cells. *J Biomech Eng*. Feb 1 2017;139(2):0210051-9. doi:10.1115/1.4035121
- 13. Mayor R, Etienne-Manneville S. The front and rear of collective cell migration. *Nat Rev Mol Cell Biol.* Feb 2016;17(2):97-109. doi:10.1038/nrm.2015.14
- 14. Giannone G, Dubin-Thaler BJ, Rossier O, et al. Lamellipodial actin mechanically links myosin activity with adhesion-site formation. *Cell*. Feb 9 2007;128(3):561-75. doi:10.1016/j.cell.2006.12.039
- 15. Schaks M, Giannone G, Rottner K. Actin dynamics in cell migration. *Essays Biochem*. Oct 31 2019;63(5):483-495. doi:10.1042/EBC20190015
- 16. Machacek M, Hodgson L, Welch C, et al. Coordination of Rho GTPase activities during cell protrusion. *Nature*. Sep 3 2009;461(7260):99-103. doi:10.1038/nature08242
- 17. Tkachenko E, Sabouri-Ghomi M, Pertz O, et al. Protein kinase A governs a RhoA-RhoGDI protrusion-retraction pacemaker in migrating cells. *Nat Cell Biol.* Jun 2011;13(6):660-7. doi:10.1038/ncb2231
- 18. Tsai FC, Kuo GH, Chang SW, Tsai PJ. Ca2+ signaling in cytoskeletal reorganization, cell migration, and cancer metastasis. *Biomed Res Int.* 2015;2015:409245. doi:10.1155/2015/409245
- 19. Tsai FC, Seki A, Yang HW, et al. A polarized Ca2+, diacylglycerol and STIM1 signalling system regulates directed cell migration. *Nat Cell Biol*. Feb 2014;16(2):133-44. doi:10.1038/ncb2906

- 20. Yang S, Huang XY. Ca2+ influx through L-type Ca2+ channels controls the trailing tail contraction in growth factor-induced fibroblast cell migration. *J Biol Chem.* Jul 22 2005;280(29):27130-7. doi:10.1074/jbc.M501625200
- 21. Webb DJ, Parsons JT, Horwitz AF. Adhesion assembly, disassembly and turnover in migrating cells -- over and over again. *Nat Cell Biol*. Apr 2002;4(4):E97-100. doi:10.1038/ncb0402-e97
- 22. Burnette DT, Manley S, Sengupta P, et al. A role for actin arcs in the leading-edge advance of migrating cells. *Nat Cell Biol*. Apr 2011;13(4):371-81. doi:10.1038/ncb2205
- 23. Berridge MJ. Inositol trisphosphate and calcium signalling. *Nature*. Jan 28 1993;361(6410):315-25. doi:10.1038/361315a0
- 24. Keizer J, Levine L. Ryanodine receptor adaptation and Ca2+(-)induced Ca2+ release-dependent Ca2+ oscillations. *Biophys J*. Dec 1996;71(6):3477-87. doi:10.1016/S0006-3495(96)79543-7
- 25. Larsson C. Protein kinase C and the regulation of the actin cytoskeleton. *Cell Signal*. Mar 2006;18(3):276-84. doi:10.1016/j.cellsig.2005.07.010
- 26. Tsai FC, Meyer T. Ca2+ pulses control local cycles of lamellipodia retraction and adhesion along the front of migrating cells. *Curr Biol*. May 8 2012;22(9):837-42. doi:10.1016/j.cub.2012.03.037
- 27. Vicente-Manzanares M, Ma X, Adelstein RS, Horwitz AR. Non-muscle myosin II takes centre stage in cell adhesion and migration. *Nat Rev Mol Cell Biol*. Nov 2009;10(11):778-90. doi:10.1038/nrm2786
- 28. Kaya M, Tani Y, Washio T, Hisada T, Higuchi H. Coordinated force generation of skeletal myosins in myofilaments through motor coupling. *Nat Commun.* Jul 6 2017;8:16036. doi:10.1038/ncomms16036
- 29. Middelbeek J, Kuipers AJ, Henneman L, et al. TRPM7 is required for breast tumor cell metastasis. *Cancer Res.* Aug 15 2012;72(16):4250-61. doi:10.1158/0008-5472.CAN-11-3863
- 30. Kasturi R, Vasulka C, Johnson JD. Ca2+, caldesmon, and myosin light chain kinase exchange with calmodulin. *J Biol Chem*. Apr 15 1993;268(11):7958-64.
- 31. Liou J, Kim ML, Heo WD, et al. STIM is a Ca2+ sensor essential for Ca2+-store-depletion-triggered Ca2+ influx. *Curr Biol.* Jul 12 2005;15(13):1235-41. doi:10.1016/j.cub.2005.05.055
- 32. Hammad AS, Machaca K. Store Operated Calcium Entry in Cell Migration and Cancer Metastasis. *Cells*. May 19 2021;10(5)doi:10.3390/cells10051246
- 33. D'Souza RS, Lim JY, Turgut A, et al. Calcium-stimulated disassembly of focal adhesions mediated by an ORP3/IQSec1 complex. *Elife*. Apr 1 2020;9doi:10.7554/eLife.54113
- 34. Franco SJ, Huttenlocher A. Regulating cell migration: calpains make the cut. *J Cell Sci.* Sep 1 2005;118(Pt 17):3829-38. doi:10.1242/jcs.02562
- 35. Bhatt A, Kaverina I, Otey C, Huttenlocher A. Regulation of focal complex composition and disassembly by the calcium-dependent protease calpain. *J Cell Sci.* Sep 1 2002;115(Pt 17):3415-25. doi:10.1242/jcs.115.17.3415
- 36. Leybaert L, Sanderson MJ. Intercellular Ca(2+) waves: mechanisms and function. *Physiol Rev.* Jul 2012;92(3):1359-92. doi:10.1152/physrev.00029.2011
- 37. Ross WN. Understanding calcium waves and sparks in central neurons. *Nat Rev Neurosci*. Feb 8 2012;13(3):157-68. doi:10.1038/nrn3168

- 38. Wei C, Wang X, Chen M, Ouyang K, Song LS, Cheng H. Calcium flickers steer cell migration. *Nature*. Feb 12 2009;457(7231):901-5. doi:10.1038/nature07577
- 39. Ellefsen KL, Holt JR, Chang AC, et al. Myosin-II mediated traction forces evoke localized Piezo1-dependent Ca(2+) flickers. *Commun Biol.* 2019;2:298. doi:10.1038/s42003-019-0514-3
- 40. Ranade SS, Qiu Z, Woo S-H, et al. Piezo1, a mechanically activated ion channel, is required for vascular development in mice. *Proceedings of the National Academy of Sciences*. 2014;111(28):10347-10352. doi:doi:10.1073/pnas.1409233111 %U https://www.pnas.org/doi/abs/10.1073/pnas.1409233111
- 41. Botello-Smith WM, Jiang W, Zhang H, et al. A mechanism for the activation of the mechanosensitive Piezo1 channel by the small molecule Yoda1. *Nat Commun*. Oct 3 2019;10(1):4503. doi:10.1038/s41467-019-12501-1
- 42. Helassa N, Zhang XH, Conte I, et al. Fast-Response Calmodulin-Based Fluorescent Indicators Reveal Rapid Intracellular Calcium Dynamics. *Sci Rep.* Nov 3 2015;5:15978. doi:10.1038/srep15978
- 43. Chen TW, Wardill TJ, Sun Y, et al. Ultrasensitive fluorescent proteins for imaging neuronal activity. *Nature*. Jul 18 2013;499(7458):295-300. doi:10.1038/nature12354
- 44. Kiepas A, Voorand E, Mubaid F, Siegel PM, Brown CM. Optimizing live-cell fluorescence imaging conditions to minimize phototoxicity. *J Cell Sci*. Feb 21 2020;133(4)doi:10.1242/jcs.242834
- 45. Ettinger A, Wittmann T. Fluorescence live cell imaging. *Methods Cell Biol.* 2014;123:77-94. doi:10.1016/B978-0-12-420138-5.00005-7
- 46. Boyat AK, Joshi BK. A review paper: noise models in digital image processing. *arXiv* preprint arXiv:150503489. 2015;
- 47. Laine RF, Jacquemet G, Krull A. Imaging in focus: An introduction to denoising bioimages in the era of deep learning. *Int J Biochem Cell Biol*. Nov 2021;140:106077. doi:10.1016/j.biocel.2021.106077
- 48. Alkinani MH, El-Sakka MR. Patch-based models and algorithms for image denoising: a comparative review between patch-based images denoising methods for additive noise reduction. *EURASIP J Image Video Process*. 2017;2017(1):58. doi:10.1186/s13640-017-0203-4
- 49. Buades A, Coll B, Morel JM. A non-local algorithm for image denoising. 2005:60-65 vol. 2.
- 50. Dabov K, Foi A, Katkovnik V, Egiazarian K. Image denoising by sparse 3-D transform-domain collaborative filtering. *IEEE Trans Image Process*. Aug 2007;16(8):2080-95. doi:10.1109/tip.2007.901238
- 51. Morales EF, Escalante HJ. Chapter 6 A brief introduction to supervised, unsupervised, and reinforcement learning. In: Torres-García AA, Reyes-García CA, Villaseñor-Pineda L, Mendoza-Montoya O, eds. *Biosignal Processing and Classification Using Computational Learning and Intelligence*. Academic Press; 2022:111-129.
- 52. Weigert M, Schmidt U, Boothe T, et al. Content-aware image restoration: pushing the limits of fluorescence microscopy. *Nat Methods*. Dec 2018;15(12):1090-1097. doi:10.1038/s41592-018-0216-7
- 53. Chaudhary S, Moon S, Lu H. Fast, efficient, and accurate neuro-imaging denoising via supervised deep learning. *Nature Communications*. 2022/09/02 2022;13(1):5165. doi:10.1038/s41467-022-32886-w

- 54. Krull A, Buchholz T-O, Jug F. Noise2void-learning denoising from single noisy images. 2019:2129-2137.
- 55. Lehtinen J, Munkberg J, Hasselgren J, et al. Noise2Noise: Learning image restoration without clean data. *arXiv preprint arXiv:180304189*. 2018;
- 56. Prakash M, Krull A, Jug F. Fully unsupervised diversity denoising with convolutional variational autoencoders. *arXiv preprint arXiv:200606072*. 2020;
- 57. Prakash M, Delbracio M, Milanfar P, Jug F. Interpretable unsupervised diversity denoising and artefact removal. *arXiv preprint arXiv:210401374*. 2021;
- 58. Batson J, Royer L. Noise2self: Blind denoising by self-supervision. PMLR; 2019:524-533 %@ 2640-3498.
- 59. Li X, Zhang G, Wu J, et al. Reinforcing neuron extraction and spike inference in calcium imaging using deep self-supervised denoising. *Nat Methods*. Nov 2021;18(11):1395-1400. doi:10.1038/s41592-021-01225-0
- 60. Lecoq J, Oliver M, Siegle JH, Orlova N, Ledochowitsch P, Koch C. Removing independent noise in systems neuroscience data using DeepInterpolation. *Nat Methods*. Nov 2021;18(11):1401-1408. doi:10.1038/s41592-021-01285-2
- 61. Berridge MJ, Lipp P, Bootman MD. The versatility and universality of calcium signalling. *Nat Rev Mol Cell Biol.* Oct 2000;1(1):11-21. doi:10.1038/35036035
- 62. Grienberger C, Konnerth A. Imaging calcium in neurons. *Neuron*. Mar 8 2012;73(5):862-85. doi:10.1016/j.neuron.2012.02.011
- 63. Madisen L, Garner AR, Shimaoka D, et al. Transgenic mice for intersectional targeting of neural sensors and effectors with high specificity and performance. *Neuron*. Mar 4 2015;85(5):942-58. doi:10.1016/j.neuron.2015.02.022
- 64. Li X, Li Y, Zhou Y, et al. Real-time denoising enables high-sensitivity fluorescence time-lapse imaging beyond the shot-noise limit. *Nat Biotechnol*. Feb 2023;41(2):282-292. doi:10.1038/s41587-022-01450-8
- 65. Hayer A, Shao L, Chung M, et al. Engulfed cadherin fingers are polarized junctional structures between collectively migrating endothelial cells. *Nat Cell Biol*. Dec 2016;18(12):1311-1323. doi:10.1038/ncb3438
- 66. Kingma DP. Adam: a method for stochastic optimization. *arXiv preprint arXiv:14126980*. 2014:
- 67. Bradski G. The OpenCV library. Dr Dobb's Journal of Software Tools. 2000;
- 68. Harris CR, Millman KJ, van der Walt SJ, et al. Array programming with NumPy. *Nature*. Sep 2020;585(7825):357-362. doi:10.1038/s41586-020-2649-2
- 69. Laissue PP, Alghamdi RA, Tomancak P, Reynaud EG, Shroff H. Assessing phototoxicity in live fluorescence imaging. *Nat Methods*. Jun 29 2017;14(7):657-661. doi:10.1038/nmeth.4344
- 70. Zhang Y, Zhang G, Han X, et al. Rapid detection of neurons in widefield calcium imaging datasets after training with synthetic data. *Nat Methods*. May 2023;20(5):747-754. doi:10.1038/s41592-023-01838-7
- 71. Zhang Y, Rozsa M, Liang Y, et al. Fast and sensitive GCaMP calcium indicators for imaging neural populations. *Nature*. Mar 2023;615(7954):884-891. doi:10.1038/s41586-023-05828-9